DESIGN OPTIMIZATION OF TOOL EXTENSION COMPONENTS IN MACHINE TOOL ASSEMBLIES BASED ON THE ABSORBER EFFECT BETWEEN SUBCOMPONENT MODES

A THESIS SUBMITTED TO
THE GRADUATE SCHOOL OF NATURAL AND APPLIED SCIENCES
OF
MIDDLE EAST TECHNICAL UNIVERSITY

BY

HATICE ELIF TOLA

IN PARTIAL FULFILLMENT OF THE REQUIREMENTS
FOR
THE DEGREE OF MASTER OF SCIENCE
IN
MECHANICAL ENGINEERING

SEPTEMBER 2022

Approval of the thesis:

DESIGN OPTIMIZATION OF TOOL EXTENSION COMPONENTS IN MACHINE TOOL ASSEMBLIES BASED ON THE ABSORBER EFFECT BETWEEN SUBCOMPONENT MODES

submitted by **HATICE ELIF TOLA** in partial fulfillment of the requirements for the degree of **Master of Science in Mechanical Engineering Department, Middle East Technical University** by,

Prof. Dr. Halil Kalıpçılar
Dean, Graduate School of **Natural and Applied Sciences** _____

Prof. Dr. M.A. Sahir Arıkan
Head of Department, **Mechanical Engineering** _____

Assist. Prof. Dr. Orkun Özşahin
Supervisor, **Mechanical Engineering, METU** _____

Examining Committee Members:

Assoc. Prof. Dr. Mehmet Bülent Özer
Mechanical Engineering, METU _____

Assist. Prof. Dr. Orkun Özşahin
Mechanical Engineering, METU _____

Assist. Prof. Dr. Hakan Çalışkan
Mechanical Engineering, METU _____

Assist. Prof. Dr. Gökhan Özgen
Mechanical Engineering, METU _____

Assist. Prof. Dr. Samet Akar
Mechanical Engineering, Çankaya University _____

Date:

I hereby declare that all information in this document has been obtained and presented in accordance with academic rules and ethical conduct. I also declare that, as required by these rules and conduct, I have fully cited and referenced all material and results that are not original to this work.

Name, Surname: Hatice Elif Tola

Signature :

ABSTRACT

DESIGN OPTIMIZATION OF TOOL EXTENSION COMPONENTS IN MACHINE TOOL ASSEMBLIES BASED ON THE ABSORBER EFFECT BETWEEN SUBCOMPONENT MODES

Tola, Hatice Elif
M.S., Department of Mechanical Engineering
Supervisor: Assist. Prof. Dr. Orkun Özşahin

September 2022, 78 pages

Regenerative vibrations, called chatter, are a major problem limits productivity due to poor surface finish, low material removal rates and decrease in life of machine tool and equipment. Stability lobe diagrams are graphs that give a stable cutting limit at a given spindle speed, developed by the researchers as a chatter prevention tool. Various methods have been investigated to increase the critical cutting limit and suppress the most flexible mode in the machine tool frequency response function(FRF). Tuned mass dampers(TMD) are one of the most widely used tools which achieve vibration attenuation by matching its natural frequency with the system's. This absorber effect can also be obtained by macthing the modes of the subcomponents of the machine center. A new component can be introduced to the system when modification of the subcomponents such as holder and tool is inconvenient. In this thesis, optimal designs for tool extension component aiming absorber effect is investigated. Dynamic properties of the spindle-holder assembly are acquired by impact hammer tests. Spindle is identified by FRF de-coupling method based on the experimental FRF data of spindle-holder assembly. After FRFs of each subcomponent is obtained, optimal design parameters of the extension and tuning of the extension-tool assembly

is investigated to have absorber effect by simulations.

Keywords: Chatter Stability, Machine Tool Dynamics, Spindle Identification, Design Optimization

ÖZ

ALT BİLEŞEN MODLARI ARASINDAKİ SÖNÜMLEYİCİ ETKİYE DAYALI OLARAK TAKIM TEZGAHI MONTAJLARINDAKİ TAKIM UZATMA BİLEŞENLERİNİN TASARIM OPTİMİZASYONU

Tola, Hatice Elif
Yüksek Lisans, Makina Mühendisliği Bölümü
Tez Yöneticisi: Dr. Öğr. Üyesi. Orkun Özşahin

Eylül 2022 , 78 sayfa

Tırlama olarak adlandırılan yineleyen titreşimler, düşük yüzey kalitesi, düşük talaş kaldırma oranları ve takım tezgahı ve ekipmanın ömrünün azalması nedeniyle üretkenliği sınırlayan önemli bir sorundur. Kararlılık diyagramları, araştırmacılar tarafından bir tırlama önleme aracı olarak geliştirilen, belirli bir iş mili hızında kararlı bir kesme derinliği veren grafiklerdir. Takım tezgahı frekans tepki fonksiyonunda(FTF) kritik kesme derinliğini artırmak ve en esnek modu bastırmak için çeşitli yöntemler araştırılmıştır. Ayarlı kütle sönümleyici(AKS), doğal frekansını sisteminki ile eşleştirerek titreşim azaltma sağlayan en yaygın olarak kullanılan araçlardan biridir. Bu sönümleyici etki, işleme merkezinin alt bileşenlerinin modları eşleştirilerek de elde edilebilir. Takım tutucu ve takım gibi alt bileşenlerin modifikasyonunun uygun olmadığı durumlarda sisteme yeni bir bileşen eklenebilir. Bu tezde, takım uzatma bileşenleri için titreşim sönümleme hedefiyle optimal tasarımlar araştırılmıştır. Mil-takım tutucu tertibatının dinamik özellikleri, darbe çekiç testleri ile elde edilir. İş mili dinamiği, iş mili-takım tutucu montajının deneysel FTF'lerinden FTF ayırma yöntemiyle

ayrılmasıyla tanımlanmıştır. Her bir alt bileşenin FTF'leri elde edildikten sonra simülasyonlar ile takım uzatıcının optimal tasarım parametreleri ve takım ve takım uzatıcı montajının ayarlanması soğurucu etkiye sahip olacak şekilde araştırılmıştır.

Anahtar Kelimeler: Tırlama Kararlılığı, Tezgah Dinamiği, İş Mili Tanımlama, Tasarım Optimizasyonu

To my Family

ACKNOWLEDGMENTS

I would like to express my sincere appreciation to my supervisor Dr. Orkun Özşahin his excellent supervision, valuable advices and critism, support and gudiance throughout all stages of the study.

I would like to thank Gamze Karataş for her effort and contribution throughout the thesis. I am grateful for her valuable suggestions and comments.

I also would like to thank my beloved friends Hatem Ak, Feyza Pirim, Merve Saraç, Hatun Taşkaya, Denge Uzel and Hilal Köksal for their support and the enjoyable time spent together. My special thanks to Mert Demirel for being always there for me whenever I needed and his unconditional support.

I would like to give my deepest gratitude to my mother Zekiye Tola and my father Abdullah Tola for their endless love and support thoughout my entire life. Special thanks to my brother Ahmet Çetin Tola, I am very grateful for his company.

TABLE OF CONTENTS

ABSTRACT v

ÖZ vii

ACKNOWLEDGMENTS x

TABLE OF CONTENTS xi

LIST OF TABLES xiv

LIST OF FIGURES xv

LIST OF ABBREVIATIONS xx

LIST OF SYMBOLS xxi

CHAPTERS

1 INTRODUCTION 1

1.1 Literature Review 1

1.2 Objective of the Thesis 5

1.3 Outline of the Thesis 6

2 MODELING OF SPINDLE-HOLDER-EXTENSION-TOOL ASSEMBLY . 9

2.1 Timoshenko Beam Theory 9

2.1.1 Eigen Value Problem of Timoshenko Beam Theory 10

2.1.2 Receptance of Free-Free Timoshenko Beam 13

2.2 Receptance Coupling Method 14

2.2.1 Receptance Coupling of Two Segments 14

2.3 Identification of the Spindle System 16

2.3.1 Mathematical Model 17

2.4 Construction of the Spindle-Holder-Extension-Tool Assembly by Receptance Coupling 19

2.5 FRF Tuning Methodology 21

3 EXPERIMENTAL VERIFICATION 23

3.1 Introduction 23

3.2 Experimental Setup 23

3.3 Impact Hammer Test and Measuring Equipment 26

3.4 Experimental Results 29

3.4.1 Holder 1 29

3.4.2 Holder 2 32

3.4.3 Holder 3 and Extension 36

3.4.4 Prediction of Holder-Extension Tip FRFs Using Identified Spindles 38

3.4.5 Holder 3-Extension and Tool 43

4 SENSITIVITY ANALYSIS IN SPINDLE - HOLDER - EXTENSION - TOOL ASSEMBLY 47

4.1 Investigation of the Effects of the Interface Dynamics 47

4.1.1 Effect of Holder-Extension Interface Dynamics 47

4.1.2 Effect of Extension-Tool Interface Dynamics 50

4.2 Effect of the Change of Extension Diameter 51

4.2.1 Diameter Increase of Segments 10 and 11 51

4.2.2 Diameter Increase of Segments 8 and 9 54

4.2.3 Diameter Increase of Segments 6 and 7 56

4.2.4 Diameter Increase of Segments 8,9,10 and 11 58

4.2.5 Diameter Increase of Segments 5 - 11 60

4.3 Effect of the Tool Overhang Length 63

4.4 Effect of the Simultaneous Change of the Extension and Tool Overhang Length 64

4.4.1 Case 1: Extension Length = 100 mm and Tool Overhang Length = 36 mm 65

4.4.2 Case 2: Extension Length = 105 mm and Tool Overhang Length = 28 mm 66

4.4.3 Case 3: Extension Length = 98 mm and Tool Overhang Length = 40 mm 67

5 SUMMARY AND CONCLUSION 71

5.1 Summary of the Thesis 71

5.2 Conclusions 72

5.3 Future Work 73

REFERENCES 75

LIST OF TABLES

TABLES

Table 3.1 Dimensions of Holder 1 Segments 30

Table 3.2 Dimensions of Holder 2 Segments 33

Table 3.3 Dimensions of Holder 3 Segments 36

Table 3.3 Dimensions of Holder 3 Segments Continued 36

Table 3.4 Elastic Parameters of Holder 3 - Extension Assembly 37

Table 3.4 Elastic Parameters of Holder 3 - Extension Assembly for Spindle 1 - Holder 3 - Extension Coupling 42

Table 3.5 Elastic Parameters Between Holder 3 - Extension Assembly 46

Table 4.1 Identified Elastic Parameters Between Holder 3 - Extension 48

Table 4.2 Identified Elastic Parameters Between Extension - Tool 48

LIST OF FIGURES

FIGURES

Figure 1.1 Stability Lobe Diagram 2

Figure 2.1 Deformed Timoshenko Beam 9

Figure 2.2 Uniform Timoshenko Beam with Free-Free End Conditions . . . 13

Figure 2.3 Rigid Coupling of Two Uniform Timoshenko Beams 15

Figure 2.4 Beam with Tapered Profile 16

Figure 2.5 FRF Decoupling Method for Identification of the Spindle Dynamics [39] 17

Figure 2.6 Spindle-holder-extension-tool Assembly 19

Figure 2.7 SHET assembly modeled as three substructures 21

Figure 3.1 Technical Drawing and Photograph of Holder 1 24

Figure 3.2 Technical Drawing and Photograph of Holder 2 24

Figure 3.3 Shrink fit clamping between a holder and a tool 25

Figure 3.4 Technical Drawing and Photograph of Holder 3 and Extension . 25

Figure 3.4 Technical Drawing and Photograph of Holder 3 and Extension . 26

Figure 3.5 Measuring Equipment Used in Modal Testing 26

Figure 3.6 Experimental Setup of Holder 1 27

Figure 3.7 Experimental Setup of Holder 2 27

Figure 3.8 Experimental Setup of Holder 3, Extension and Tool 28

Figure 3.9 Holder 1 Modeled with Cylindrical Segments 29

Figure 3.9 Holder 1 Modeled with Cylindrical Segments 30

Figure 3.10 Identified Dynamics of Spindle by Using FRF Data of Holder 1 . 31

Figure 3.11 Spindle-Holder 1 FRF 31

Figure 3.11 Spindle-Holder 1 FRF 32

Figure 3.12 Holder 2 with 11 Segments 33

Figure 3.13 Identified Dynamics of Spindle by Using FRF Data of Holder 2 . 33

Figure 3.14 Spindle-Holder 2 FRF 34

Figure 3.15 Identified Spindle FRFs 35

Figure 3.16 Holder 3 and Extension as a Unified Model 36

Figure 3.17 Holder 3 and Extension FRF with Free-Free Boundary Conditions 37

Figure 3.18 Comparison of Identified Spindles 38

Figure 3.19 Spindle Identified Using Holder 1 Coupled with Holder 2 FRF . 39

Figure 3.20 Spindle Identified Using Holder 1 Coupled with Holder 3 FRF . 40

Figure 3.21 Spindle Identified Using Holder 1 Coupled with Holder 3 FRF in Linear Scale 41

Figure 3.22 Spindle Identified Using Holder 1 Coupled with Holder 3-Extension FRF (Elastic Contact Between Holder 3-Extension) 42

Figure 3.22 Spindle Identified Using Holder 1 Coupled with Holder 3-Extension FRF (Elastic Contact Between Holder 3-Extension) 43

Figure 3.23 Tool Tip FRF 44

Figure 3.24 Tool Tip FRF with Elastic Contact Between Holder and Extension 45

Figure 4.1 Change of Holder 3-Extension Contact Interface Length 48

Figure 4.1 Change of Holder 3-Extension Contact Interface Length - Continued 49

Figure 4.2 Effect of Holder 3-Extension Contact Interface Length on Tool Tip FRF 49

Figure 4.3 Incremental Tool Length Increase inside the Extension 50

Figure 4.4 Effect of Extension-Tool Contact Interface Length on Tool Tip FRF 51

Figure 4.5 Segments of the Extension with Increased Diameter 52

Figure 4.6 Tool Tip FRF with Increased Diameter of Segments 10 and 11 . 52

Figure 4.7 Maximum Tool Tip FRF Amplitude with Changing Segment Diameter 53

Figure 4.8 Comparison of Stability Lobe Diagrams for Initial Geometry of Extension and Increased Diameter of the Segments 10 and 11 to 60 mm 53

Figure 4.9 Segments of the Extension with Increased Diameter 54

Figure 4.10 Tool Tip FRF with Increased Diameter of Segments 8 and 9 . . . 54

Figure 4.11 Maximum Tool Tip FRF Amplitude with Changing Segment Diameter 55

Figure 4.12 Comparison of Stability Lobe Diagrams for Initial Geometry of Extension and Increased Diameter of the Segments 8 and 9 to 60 mm . . 55

Figure 4.13 Segments of the Extension with Increased Diameter 56

Figure 4.14 Tool Tip FRF with Increased Diameter of Segments 6 and 7 . . . 57

Figure 4.15 Maximum Tool Tip FRF Amplitude with Changing Segment Diameter 57

Figure 4.16 Comparison of Stability Lobe Diagrams for Initial Geometry of Extension and Increased Diameter of the Segments 6 and 7 to 50 mm . . 58

Figure 4.17 Segments of the Extension with Increased Diameter 58

Figure 4.18 Tool Tip FRF with Increased Diameter of Segments 8,9,10 and 11 59

Figure 4.19 Maximum Tool Tip FRF Amplitude with Changing Segment Diameter 59

Figure 4.20 Comparison of Stability Lobe Diagrams for Initial Geometry of Extension and Increased Diameter of the Segments 8, 9, 10 and 11 to 55 mm 60

Figure 4.21 Segments of the Extension with Increased Diameter 61

Figure 4.22 Tool Tip FRF with Increased Diameter of Segments 5-11 61

Figure 4.23 Maximum Tool Tip FRF Amplitude with Changing Segment Diameter 62

Figure 4.24 Comparison of Stability Lobe Diagrams for Initial Geometry of Extension and Increased Diameter of the All Segments to 60 mm 62

Figure 4.25 Tool Tip FRF Amplitude with Changing Tool Overhang Length . 63

Figure 4.26 Maximum Tool Tip Amplitude with Changing Tool Overhang Length 64

Figure 4.27 Maximum Tool Tip FRF Amplitude obtained for Combinations of Extension Length and Tool Overhang Length 64

Figure 4.28 Amplitude of Tool Tip FRF for Case 1 65

Figure 4.29 Stability Lobe Diagram for Case 1 66

Figure 4.30 Amplitude of Tool Tip FRF for Case 2 67

Figure 4.31 Stability Lobe Diagram for Case 2 67

Figure 4.32 Amplitude of Tool Tip FRF for Case 3 68

Figure 4.33 Stability Lobe Diagram for Case 3 68

LIST OF ABBREVIATIONS

DOF	Degree of Freedom
FRF	Frequency Response Function
MRR	Material Removal Rate
SDOF	Single Degree of Freedom
SLD	Stability Lobe Diagram
TMD	Tuned Mass Damper

LIST OF SYMBOLS

a_{lim}	Chatter-free depth of cut
a_{xx}	Dynamic milling force coefficient
K_t	Translational cutting force
$Re[G(\omega)]$	Real part of the tool tip Frequency Response Function
ω_c	Chatter frequency
t	Time
x	Axial direction
$y(x,t)$	Displacement in transverse direction
$\beta(x,t)$	Rotation angle due to shear distortion
$\psi(x,t)$	Rotation angle due to bending
$V(x,t)$	Shear force
$M(x,t)$	Bending moment
k'	Shear coefficient
A	Cross-sectional area of the beam
G	Shear modulus
ρ	Density
E	Young's modulus
I	Area moment of inertia
L	Length of the beam
ω	Excitation frequency
ω_r	R-th elastic mode
$\bar{Y_r}(x)$	Eigenfunction of transverse displacement(not normalized)
$\bar{\psi_r}(x)$	Eigenfunction of rotational displacement(not normalized)

$\phi_r(x)$	Mass normalized transverse displacement eigenfunction
$\varphi_r(x)$	Mass normalized bending rotation eigenfunction
η_r	r-th mode time domain modal coordinate
H_{jk}	Transverse displacement at coordinate i due to unit harmonic force excitation at point j
L_{jk}	Transverse displacement at coordinate i due to unit harmonic moment excitation at point j
N_{jk}	Rotational displacement at coordinate i due to unit harmonic force excitation at point j
P_{jk}	Rotational displacement at coordinate i due to unit harmonic moment excitation at point j
γ	Loss factor
k_y	Translational stiffness
k_θ	Rotational stiffness
c_y	Translational stiffness
c_θ	Rotational stiffness
$\phi(x)$	Objective function

CHAPTER 1

INTRODUCTION

1.1 Literature Review

Chatter is a phenomenon that leads to certain limitations in the machining process due to self-excited vibration. Preventing desired surface finish, decreasing the life of the tool and machine parts and reducing material removal rate are some of the damages caused by chatter. Chatter suppression techniques have been investigated for almost 70 years since high productivity rates, accuracy and stability are desired elements in the progress of the machining industry [1], [2].

Stability lobe diagram(SLD) is an instrument for selecting the depth of cut and spindle speed in order to avoid chatter that was introduced by Tobias and Fishwick [3]. An example of a stability lobe diagram is shown in Figure 1.1. The critical depth of cut to avoid the unstable region for milling of a single degree of freedom structure(SDOF) is given as [4]

$$a_{lim} = \frac{2\pi}{a_{xx} K_t Re[G_{xx}(i\omega_c)]} \tag{1.1}$$

where K_t is translational cutting constant, a_{xx} is dynamic milling force coefficient and $Re[G_{xx}(i\omega_c)]$ refers to real part of the tool point Frequency Response Function(FRF) at the chatter frequency(ω_c). To calculate the stability diagrams, effects of the system dynamics at the tool point are needed to be known as Equation 1.1 suggests. Spindle, tool holder and tool are the common components that comprise the system of a machining center therefore, in addition to their individual dynamics, interaction between them needs to be taken into account while obtaining the tool point FRF. Impact testing and modal analysis are the commonly used methods for obtaining the system dynamics and tool tip FRF. Impact testing requires measurement of the response data

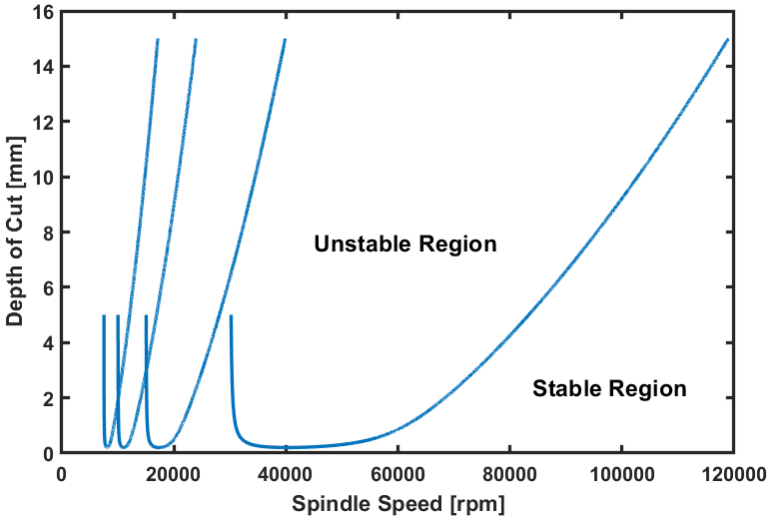


Figure 1.1: Stability Lobe Diagram

of the interested component or a system by an accelerometer which is located at the same position as the excitation point. However, it requires repeating the test whenever the system components or assembly changes since impact testing is unique for each test layout. For this reason, more time efficient and practical methods have been interested by the researchers.

To eliminate the experimental measurements of the tool point FRF for each holder-tool combinations, Schmitz et al. proposed a method for predicting dynamics of a high speed machining assembly that couples analytically calculated response of the tool with the experimentally measured response of holder and spindle [5–7]. They modeled the tool as a free-free beam and spindle-holder assembly was subjected to an impact hammer test to measure FRFs. As a result, assembly's dynamic FRF at the tool tip was accurately predicted by receptance coupling substructure analysis. Tool was modeled as a free-free uniform Euler-Bernoulli beam and elastic contact parameters were extracted from a measurement of the spindle-holder-tool assembly which are specific to the tool in [8] for predicting tool point FRF by receptance coupling.

Ertürk et al. [9] analytically modeled not only tool but also holder and spindle by using uniform free-free Timoshenko beam since Euler-Bernoulli model is insufficient due to omission of the effects of rotary inertia and shear deformation. They modeled all components as multi-segmented Timoshenko beams and elastically coupled

by receptance coupling method, and it was shown that Timoshenko beam gives better results than Euler-Bernoulli theory especially in high frequency region. Effects of bearing dynamics in the spindle and interface dynamics between the components of the assembly were studied, and analytical model employing Timoshenko beam theory was experimentally verified in [10]. Özşahin et al. extended the analytical model of the components by including gyroscopic effects to Timoshenko beam theory and showed the significance of the effect of speed depended bearing parameters on predicting tool tip FRF under operational conditions [11].

For analytical calculations and experimental measurements of the tool tip FRF to provide adequate fit, the contact parameters and elastic properties of the assembly must be included in the model. Stiffness and damping properties at the connection points were semi-analytically calculated and it was assumed that contact parameters are located at a single point between junction of the two components in [5–11]. Schmitz et al. introduced third generation receptance coupling substructure analysis which includes the contact dynamics along the interface of the tool and the holder modeled as multiple connection points [12]. Ahmadi and Ahmadian [13] experimentally obtained the flexibility between spindle and holder assembly and they used analytical model of the tool to predict the tool point FRF. Results were improved by introducing distributed stiffness and damping model along the holder and tool interface instead of lumped one. An effect analysis was conducted on spindle-holder and tool assembly and it was shown that first two modes of the tool point FRF are controlled by the spindle in [14]. It was also found that rotational contact parameters have negligible effect on the tool tip FRF compared to translational ones. Özşahin et al. [15] proposed a new method to identify dynamic contact parameters at the connection points of spindle-holder and tool assemblies. Elastic receptance coupling equations were manipulated to obtain complex stiffness matrix at the spindle-holder and holder-tool interfaces. Furthermore, experimental verification of the approach was provided. Later, artificial neural networks theory was utilized for prediction of dynamic contact parameters by [16]. First, method proposed in [14] was used for identification of contact parameters at the holder-tool interface. Then, identified data was used for training artificial neural networks which was found out to have ability to accurately predict the contact parameters.

After identification of the dynamic parameters of the machining center is completed, these parameters are modified to avoid chatter and increase the stable cutting regions. Modification can be provided by introducing an external system to the machine tool assembly. Tuned Mass Damper(TMD) is one of the methods widely used for chatter suppression since introduced by [17] for the first time. Damping effect is obtained when the natural frequency of TMD is tuned to match with the critical frequency of the machine tool assembly [1]. Tuning of the TMD has to be done correctly since the suppression effect of the TMD has limited frequency range [18]. Therefore, optimal tuning strategies have been developed by the researchers. Sims [19] proposed an analytical solution to optimal tuning TMDs and chatter mitigation, and it was shown that critical depth of cut was improved. Negative real part of the tool tip FRF at the interface of tool and work-piece is negatively proportional to stable cutting depth. Therefore, Yang et al. [20] aimed minimizing the negative real part of the tool point FRF and utilized minimax algorithm to optimize tuning multiple TMDs. Increase in critical depth of cut provided by the method was experimentally verified. Randall et al. [21] also used minimax optimization algorithm for tuning TMDs and they were able to obtain design graphs for optimal TMD parameters. Tarng et al. [22] used piezoelectric TMD on the cutting tool in turning operation to improve chatter stability by minimizing negative real part of the tool tip response. Chatter suppression using TMD on boring bar, modeled as a Euler-Bernoulli beam, was aimed by Miguélez et al. [23]. Analytical methods developed by Den Hartog [18] and Sims [19] were used for identification of optimum parameters of TMDs and it was found that method proposed by Sims [19] gives wider stable region. Cutting tool in milling operations performs high-speed rotation unlike the cutting tools used in turning and boring bars.

Decreasing the effects of the chatter can be obtained by modifying the dynamics of the tool instead of introducing an external component to the machine center. Changing the tool dynamics by means of modification on the tool overhang length has been investigated by the researchers. Tlusty et al. [24] observed that changing the length of the end mill can lead to increase in spindle capabilities. Moreover, it was remarked that material removal rate can be increased by adjusting the tool length. Smith et al. [25] modeled the spindle systems and the tools in various lengths by finite element method and investigated the effect of the tool length on critical depth of cut and MRR

in high-speed milling. It was shown both analytically and experimentally that tool length strongly affects the dominant region on SLD which corresponds to the most flexible mode. Schmitz et al. [26] examined the effects of tool length on the cutting stability and MRR by milling experiments. Tool was modeled as a Euler-Bernoulli beam with variable length and coupled with experimental FRF of spindle-holder assembly by using RCSA. Duncan et al. [27] defined dynamic absorber effect as an outcome of an interaction between the modes related with sub-components of a machine center and provided the experimental verification. Experimental measurements showed that dynamic stiffness of the assembly at the tool tip is increased when the match between spindle-holder mode and tool mode is obtained.

Ertürk et al. [28] focused on the dynamic absorber effect by alterations on design and operational parameters of a machine tool assembly parts. It was observed that changing geometric properties of the components improves the chatter stability. Mohammadi et al. [29] proposed a systematic method to calculate the required dimensions for modal interaction. Each components of the spindle-holder-tool was examined to utilize absorber effect and analytical results were verified by impact and chatter tests. Gibbons et al. [30] introduced a new structural modification method and investigated the effect of tool-holder diameter on cutting stability in milling. It was provided to choose an optimal diameter of tool-holder by using only one experimental and analytical model. Karataş et al. [31] optimized the extension and tool overhang length for separate and simultaneous cases. It is verified by simulations that the optimization of the extension and tool lengths have suppressing effect on the chatter frequency due to absorber effect between the sub-components.

1.2 Objective of the Thesis

The objective of this thesis is to propose an optimal tool extension design in machine tool assemblies in order to absorb the mode that dominates the tool point FRF. Absorber effect is stem from interaction between the modes of sub-components of the structure which leads to improvement in the dynamic rigidity of the machine center. In literature, each components of spindle-holder-tool assembly is investigated in terms of geometric properties to achieve absorber effect. However, changing the di-

mensions of the components has certain limitations such as; spindle modification is only possible at the design stage. Thus, convenience of the solution is also an important factor. In cases where a long reach is required in milling operations, an extension piece is preferred between the holder and the tool which can be considered as low-cost and practical solution. In this thesis, dynamic properties of the spindle is identified by experimental FRF measurement of the spindle-holder assembly. Moreover, geometrical properties of the holder extension are adjusted to enable interaction between the component modes. Finally, improvement in dynamic rigidity of the machine tool assembly and increase in stable cutting region in SLD is demonstrated through simulations.

1.3 Outline of the Thesis

The outline of the thesis as follows:

In Chapter 2, background required for the modeling the spindle-holder-extension-tool assembly by using receptance coupling method and procedure for design optimization of tool extension component is built. First, Timoshenko beam theory which is used for analytical modeling of the machine tool components is explained. Then, receptance coupling method is described which is utilized for both coupling the segments of a machine tool component and the components with each other. Next, procedure follow for identification of the spindle based on experimental FRF data is explained. Finally, analytical model of the SHET assembly is constructed and FRF tuning methodology are explained.

In Chapter 3, experimental verification spindle identification is presented. First, impact hammer test is applied on the assemblies of spindle with several holders and a tool. Receptance function of the spindle is identified by de-coupling the analytically calculated receptances of the holders. Verification of the spindle dynamics is provided by comparison of the FRFs obtained from different holders. Finally, elastic contact parameters between holder-extension and extension-tool is also identified.

In Chapter 4, a sensitivity analysis of the SHET assembly is carried out. First, effect of the interface contact length between the holder-extension and extension-tool

assemblies are investigated through simulations. Furthermore, effects of the geometric properties such as overhang length and diameter of the extension and tool on the tool tip FRF is examined. Simultaneous optimization of the extension and tool overhang length is investigated. Finally, improvements obtained by the examined cases on stability lobe diagram are provided through simulations.

In Chapter 5, the summary and conclusion of the thesis is provided and suggestions regarding future work is made.

CHAPTER 2

MODELING OF SPINDLE-HOLDER-EXTENSION-TOOL ASSEMBLY

2.1 Timoshenko Beam Theory

Various beam theories have been developed for analytical modeling of the beam elements. Euler-Bernoulli beam theory is widely used in literature for modeling machine tool components as in [8, 23]. Euler-Bernoulli theory correctly reflects the dynamic properties of a beam with high slenderness ratio. However, shear deformation and rotary inertia are not included in this theory. Therefore, Euler-Bernoulli beam is inadequate for modeling machine tool components in high frequency region due to low slenderness ratio. Timoshenko introduced a beam theory by including shear deformation and rotary inertia effects [32,33] which accurately models any beam independent of its slenderness ratio. An example of Timoshenko beam element, internal forces and moments on the beam is given in Figure 2.1. In this thesis, Timoshenko beam theory is utilized for mathematically modeling of the machine tool components.

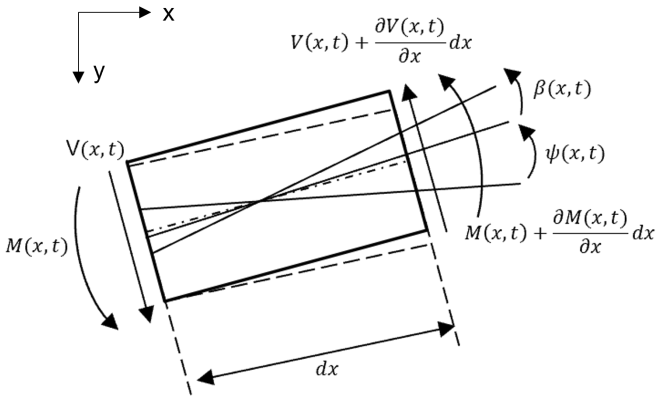


Figure 2.1: Deformed Timoshenko Beam

In Figure 2.1, the displacement variable in transverse direction is denoted by $y(x,t)$ and $\beta(x,t)$ and $\psi(x,t)$ represent distortion angle and angle of rotation due to bending, respectively. $V(x,t)$ and $M(x,t)$ symbolizes shear force and bending moment, respectively. Shear force expression differs from the shear force in Euler-Bernoulli theory since it is assumed that it occurs due to shear deformation rather than bending moment. Equation 2.1 shows shear force:

$$V(x,t) = k'.A.G.\beta(x,t) \tag{2.1}$$

where k' is the shear coefficient, A is the cross-sectional area of the beam and G is the shear modulus. Uncoupled differential equations of motion when no external force is applied on the beam can be written as follows [34]:

$$\frac{\delta^4 y(x,t)}{\delta x^4} - \left(\frac{\rho}{E} + \frac{\rho}{k'G}\right)\frac{\delta^4 y(x,t)}{\delta x^2 \delta t^2} + \frac{\rho A}{EI}.\frac{\delta^2 y(x,t)}{\delta t^2} + \frac{\rho^2}{k'EG}.\frac{\delta^4 y(x,t)}{\delta t^4} = 0 \tag{2.2}$$

$$\frac{\delta^4 \psi(x,t)}{\delta x^4} - \left(\frac{\rho}{E} + \frac{\rho}{k'G}\right)\frac{\delta^4 \psi(x,t)}{\delta x^2 \delta t^2} + \frac{\rho A}{EI}.\frac{\delta^2 \psi(x,t)}{\delta t^2} + \frac{\rho^2}{k'EG}.\frac{\delta^4 \psi(x,t)}{\delta t^4} = 0 \tag{2.3}$$

where ρ is density, *E* is Young's modulus and *I* is area moment of inertia of the cross-section of the beam.

2.1.1 Eigen Value Problem of Timoshenko Beam Theory

Shear force and bending moment are zero at the boundaries *x=0* and *x=L* for a free-free Timoshenko beam resulting four boundary conditions:

$$V(0,t) = k'AG\left(\frac{\delta y(x,t)}{\delta x} - \psi(x,t)\right)\Bigg|_{x=0} = 0 \tag{2.4}$$

$$V(L,t) = k'AG\left(\frac{\delta y(x,t)}{\delta x} - \psi(x,t)\right)\Bigg|_{x=L} = 0 \tag{2.5}$$

$$M(0,t) = EI\frac{\delta \psi(x,t)}{\delta x}\Bigg|_{x=0} = 0 \tag{2.6}$$

$$M(L,t) = EI\frac{\delta \psi(x,t)}{\delta x}\Bigg|_{x=L} = 0 \tag{2.7}$$

Equations 2.2 - 2.7 define the eigenvalue problem of uniform Timoshenko beam with free-free boundary conditions. It is assumed that response of the beam is harmonic in time domain and response equations are written as:

$$y(x,t) = \bar{y}(x)e^{i.\omega.t} \tag{2.8}$$

$$\psi(x,t) = \bar{\psi}(x)e^{i.\omega.t} \tag{2.9}$$

As a result, differential equations of motion are turned into ordinary equations:

$$\frac{d^4\bar{y}(x)}{dx^4} + \omega^2\left(\frac{\rho}{E} + \frac{\rho}{k'G}\right)\frac{d^2\bar{y}(x)}{dx^2} - \omega^2\left(\frac{\rho A}{EI} - \omega^2\frac{\rho^2}{k'EG}\right)\bar{y}(x) = 0 \tag{2.10}$$

$$\frac{d^4\bar{\psi}(x)}{dx^4} + \omega^2\left(\frac{\rho}{E} + \frac{\rho}{k'G}\right)\frac{d^2\bar{\psi}(x)}{dx^2} - \omega^2\left(\frac{\rho A}{EI} - \omega^2\frac{\rho^2}{k'EG}\right)\bar{\psi}(x) = 0 \tag{2.11}$$

By following the classical eigensolution the characteristic equation is written as [34]:

$$\begin{vmatrix} D_{11} & D_{12} \\ D_{21} & D_{22} \end{vmatrix} = D_{11}D_{22} - D_{12}D_{21} = 0 \tag{2.12}$$

where

$$D_{11} = (\alpha - \lambda).(\cos\alpha - \cosh\beta) \tag{2.13}$$

$$D_{12} = (\lambda - \alpha)\sin\alpha + \frac{\lambda\alpha}{\beta\delta}(\beta - \delta)\sinh\beta \tag{2.14}$$

$$D_{21} = -\lambda\alpha\sin\alpha + \frac{\alpha - \lambda}{\delta - \beta}\sinh\beta \tag{2.15}$$

$$D_{22} = \lambda\alpha(\cosh\beta - \cos\alpha) \tag{2.16}$$

Here, α and β are the dimensionless frequency numbers given as:

$$\alpha = \sqrt{\Omega + \varepsilon} \tag{2.17}$$

$$\beta = \sqrt{-\Omega + \varepsilon} \tag{2.18}$$

where

$$\Omega = \frac{b^2(s^2 + R^2)}{2} \tag{2.19}$$

$$\varepsilon = b\sqrt{\frac{1}{4}b^2(s^2 + R^2)^2 - (b^2s^2R^2 - 1)} \tag{2.20}$$

$$b^2 = \frac{\rho A\omega^2 L^4}{EI}, \quad s^2 = \frac{EI}{k'AGL^2}, \quad R^2 = \frac{L}{AL^2} \tag{2.21}$$

The natural frequency ω_r corresponds to the r-th elastic mode and, the dimensionless frequency numbers α_r β_r are obtained by solving the characteristic equation given by 2.12. As a result, the eigenfunctions of transverse displacement and bending rotation can be written as:

$$\bar{Y_r}(x) = A_r \left[C_1 . \sin\left(\frac{\alpha_r}{L}.x\right) + C_2 . \cos\left(\frac{\alpha_r}{L}.x\right) + C_3 . \sinh\left(\frac{\beta_r}{L}.x\right) + C_4 . \cosh\left(\frac{\beta_r}{L}.x\right) \right] \tag{2.22}$$

$$\bar{\psi_r}(x) = \frac{A_r}{L} \left[\lambda_r \left(C_1 . \cos\left(\frac{\alpha_r}{L}.x\right) - C_2 . \sin\left(\frac{\alpha_r}{L}.x\right) \right) + \delta_r \left(C_3 . \cosh\left(\frac{\beta_r}{L}.x\right) + C_4 . \sinh\left(\frac{\beta_r}{L}.x\right) \right) \right] \tag{2.23}$$

where

$$\lambda_r = \alpha_r - \frac{b^2.s^2}{\alpha_r}, \quad \delta_r = \beta_r + \frac{b^2.s^2}{\beta_r} \tag{2.24}$$

$$C_1 = L, \quad C_2 = -\frac{D_{11}}{D_{12}}, \quad C_3 = \frac{\alpha_r - \lambda_r}{\delta_r - \beta_r}, \quad C_4 = -\frac{\lambda_r.\alpha_r}{\delta_r.\beta_r}.\frac{D_{11}}{D_{12}}.C_1 \tag{2.25}$$

$(r = 1, 2, ...)$

A_r expression in Equations 2.22 and 2.23 is a constant that is obtained by the mass normalization of the eigenfunctions so that the orthogonality condition is satisfied:

$$\int_{x=0}^{L} \left\{\bar{U_s}(x)\right\}^T [M] \left\{\bar{U_r}(x)\right\} \, dx = \begin{cases} 1, & s = r \\ 0, & s \neq r \end{cases} \tag{2.26}$$

where,

$$\left\{\bar{U_r}(x)\right\} = \begin{Bmatrix} \bar{y_r}(x) \\ \bar{\psi_r}(x) \end{Bmatrix}, \qquad [M] = \begin{bmatrix} \rho.A & 0 \\ 0 & \rho.I \end{bmatrix} \tag{2.27}$$

Two rigid body modes occur because of the free-free boundary conditions. Translational rigid body mode is denoted by y_0 and rotational rigid body mode is denoted by ψ_0:

$$y_0(x) = \sqrt{\frac{1}{\rho A L}} \tag{2.28}$$

$$\psi_0(x) = \sqrt{\frac{12}{\rho A L^3}} \cdot \left(x - \frac{L}{2}\right) \tag{2.29}$$

Transverse displacement $y(x,t)$ and bending rotation displacement $\psi(x,t)$ can be expressed by utilizing the eigenfunction expansion theorem:

$$y(x,t) = \sum_{0}^{\infty} \phi_r(x).\eta_r(t) \tag{2.30}$$

$$\psi(x,t) = \sum_{0}^{\infty} \varphi_r(x).\eta_r(t) \tag{2.31}$$

Here, ϕ_r represents the mass normalized transverse displacement eigenfunction and φ_r represents the the mass normalized eigenfunction of the bending rotation. The time domain modal coordinate of the r-th mode is denoted by η_r.

2.1.2 Receptance of Free-Free Timoshenko Beam

Receptance functions relate the applied forces and moments on the beam to the translational and rotational displacement. All receptance functions can be obtained by utilizing the mass normalized eigenfunctions. The receptance functions can be written as [9]:

$$y_j = H_{jk}F_k, \qquad y_j = L_{jk}M_k \tag{2.32}$$

$$\psi_j = N_{jk}F_k, \qquad \psi_j = P_{jk}M_k, \tag{2.33}$$

where translational and rotational displacements are represented by y andψ, and the force and moment applied at the point of interest are represented by F and M, respectively. Figure 2.2 shows the location of receptance points.

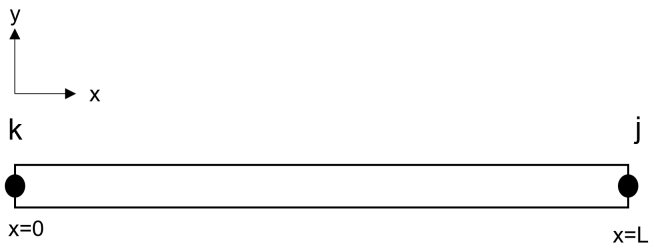


Figure 2.2: Uniform Timoshenko Beam with Free-Free End Conditions

The calculation of receptance functions of uniform free-free Timoshenko beam element is given as:

$$H_{jk} = \sum_{0}^{\infty} \frac{\phi_r(x_j).\phi_r(x_k)}{(1+i.\gamma).\omega_r^2 - \omega^2} \tag{2.34}$$

$$L_{jk} = \sum_{0}^{\infty} \frac{\phi_r(x_j).\varphi_r(x_k)}{(1+i.\gamma).\omega_r^2 - \omega^2} \tag{2.35}$$

$$N_{jk} = \sum_{0}^{\infty} \frac{\varphi_r(x_j).\phi_r(x_k)}{(1+i.\gamma).\omega_r^2 - \omega^2} \tag{2.36}$$

$$P_{jk} = \sum_{0}^{\infty} \frac{\varphi_r(x_j).\varphi_r(x_k)}{(1+i.\gamma).\omega_r^2 - \omega^2} \tag{2.37}$$

where γ is the loss factor. The formulation of the receptance matrix can be written as:

$$[B_{jk}] = \begin{bmatrix} H_{jk}^B & L_{jk}^B \\ N_{jk}^B & P_{jk}^B \end{bmatrix} \tag{2.38}$$

2.2 Receptance Coupling Method

In the previous section,receptance functions of uniform Timoshenko beam with free-free boundary conditions are defined. In this thesis, machine tool components are assumed to comprise of a finite number of uniform Timoshenko beam segments. Therefore, receptance function of each segment is calculated separately and combined by rigid receptance coupling method to obtain the receptance function of the component of interest. Then, components(holder and tool) are coupled by elastic receptance coupling by including elastic contact at the connection points to obtain the response of the machine tool assembly.

2.2.1 Receptance Coupling of Two Segments

Figure 2.3 shows rigid coupling of the two uniform segments(Block A and Block B) with free-free end-conditions to form a single part (Block C). This procedure is repeated until the machine tool component is completed. First, receptance matrices of segment A and segment B is calculated which are denoted by Equations 2.39 and 2.40, respectively.

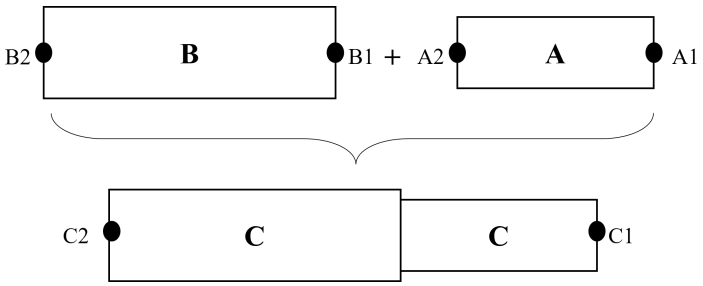


Figure 2.3: Rigid Coupling of Two Uniform Timoshenko Beams

$$[A] = \begin{bmatrix} [A_{11}] & [A_{12}] \\ [A_{21}] & [A_{22}] \end{bmatrix} \tag{2.39}$$

$$[B] = \begin{bmatrix} [B_{11}] & [B_{12}] \\ [B_{21}] & [B_{22}] \end{bmatrix} \tag{2.40}$$

Here, the point and transfer receptance functions of the end points of the segments are included in the sub-matrices:

$$[A_{jk}] = \begin{bmatrix} [H^A_{jk}] & [L^A_{jk}] \\ [N^A_{jk}] & [P^A_{jk}] \end{bmatrix} \tag{2.41}$$

$$[B_{jk}] = \begin{bmatrix} [H^B_{jk}] & [L^B_{jk}] \\ [N^B_{jk}] & [P^B_{jk}] \end{bmatrix} \tag{2.42}$$

After writing relations between the displacement and the force(or moment) for each segment, compatibility and continuity relations at the connection point are constructed:

$$\begin{Bmatrix} y_{A2} \\ \psi_{A2} \end{Bmatrix} = \begin{Bmatrix} y_{B1} \\ \psi_{B1} \end{Bmatrix} \tag{2.43}$$

$$\begin{Bmatrix} f_{A2} \\ \psi_{A2} \end{Bmatrix} = - \begin{Bmatrix} f_{B1} \\ \psi_{B1} \end{Bmatrix} \tag{2.44}$$

Point and transfer end point receptance matrices of the beam C which is combination of two segments can be written as [9]:

$$[C_{11}] = [A_{11}] - [A_{12}].\left[[A_{12}] + [B_{11}]\right]^{-1}.[A_{21}] \tag{2.45}$$

$$[C_{12}] = [A_{12}].\left[[A_{22}] + [B_{11}]\right]^{-1}.[B_{12}] \tag{2.46}$$

$$[C_{21}] = [B_{21}].\left[[A_{22}] + [B_{11}]\right]^{-1}.[A_{21}] \tag{2.47}$$

$$[C_{22}] = [B_{22}] - [B_{21}].\left[[A_{22}] + [B_{11}]\right]^{-1}.[B_{12}] \tag{2.48}$$

As a result, receptance matrix of beam C is constructed as:

$$[C] = \begin{bmatrix} [C_{11}] & [C_{12}] \\ [C_{21}] & [C_{22}] \end{bmatrix} \tag{2.49}$$

It should be noted that the machine tool components does not always uniform cross-section therefore, in such cases, component is divided into n-segments in order to obtain non-uniform profile such as tapered beam. Figure 2.4 shows the sectioning of a tapered profile beam into n number of uniform segments.

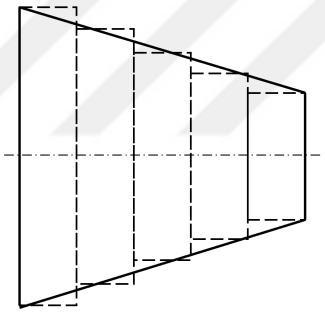


Figure 2.4: Beam with Tapered Profile

2.3 Identification of the Spindle System

The structure of the spindle can only be known with certainty by the manufacturer and the designer. Otherwise, analytical modeling methods or experimental procedures are adopted to identify the dynamics of the spindle. In this thesis, response of the spindle-holder assembly is measured by impact hammer test and dynamics of the spindle is identified by FRF decoupling method. Analytically calculated FRF of the holders are used by applying FRF decoupling method. Figure 2.5 [35] shows FRF decoupling

procedure for identification of the spindle. Here,structure A represents an arbitrary holder excluded the parts inside the spindle and structure B is the spindle.

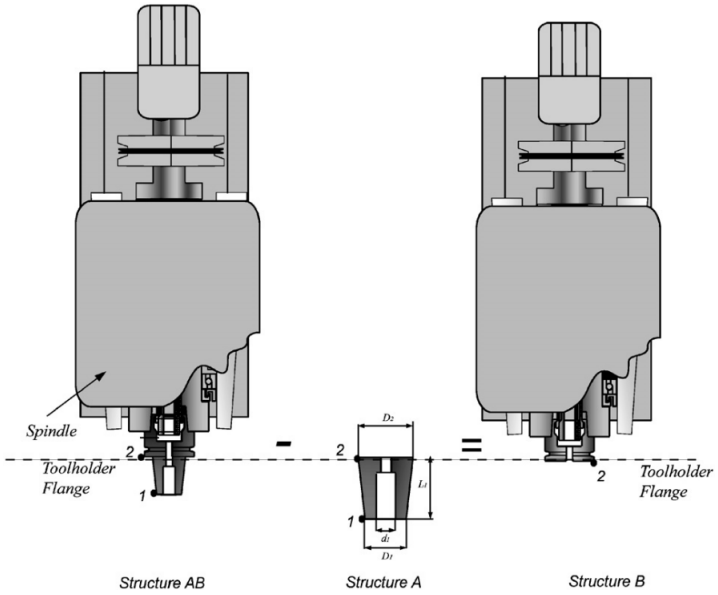


Figure 2.5: FRF Decoupling Method for Identification of the Spindle Dynamics [39]

2.3.1 Mathematical Model

It is assumed that the contact at the connection point of the two substructures is rigid, the equilibrium and compatibility equations can be written as:

$$F_2 = F_{A,2} + F_{B,2} \tag{2.50}$$

$$X_2 = X_{A,2} + X_{B,2} \tag{2.51}$$

The free-free FRF of substructure A is calculated by receptance coupling method by utilizing Timoshenko beam theory as mentioned in 2.2 and can be written as:

$$\begin{Bmatrix} X_1 \\ X_{A,2} \end{Bmatrix} = \begin{bmatrix} H_{A,11} & H_{A,12} \\ H_{A,21} & H_{A,22} \end{bmatrix} . \begin{Bmatrix} F_1 \\ F_{A,2} \end{Bmatrix} \tag{2.52}$$

where displacement vector and force vectors contain information related to both translational and rotational motion. Similarly, the FRFs of substructure B at point 2 is written as:

$$\{X_{B,2}\} = [H_{B,22}] . \{F_{B,2}\} \tag{2.53}$$

Receptance at the point 2 can be expressed as the following relation due to rigid contact:

$$H_2 = H_{A,22} + H_{B,22} \tag{2.54}$$

By using this relation receptance matrices at points 1 and 2 can eb obtained in terms of the receptance of substructure A and B [35]:

$$\begin{aligned}
[H_{11}] &= \begin{bmatrix} h_{11,FF} & h_{11,FM} \\ h_{11,MF} & h_{11,MM} \end{bmatrix} \\
&= \begin{bmatrix} h_{A11,FF} & h_{A11,FM} \\ h_{A11,MF} & h_{A11,MM} \end{bmatrix} - \begin{bmatrix} h_{A12,FF} & h_{A12,FM} \\ h_{A12,MF} & h_{A12,MM} \end{bmatrix} [H_2]^{-1} \begin{bmatrix} h_{A21,FF} & h_{A21,FM} \\ h_{A21,MF} & h_{A21,MM} \end{bmatrix}, \\
[H_{21}] &= \begin{bmatrix} h_{21,FF} & h_{21,FM} \\ h_{21,MF} & h_{21,MM} \end{bmatrix} \\
&= \begin{bmatrix} h_{A21,FF} & h_{A21,FM} \\ h_{A21,MF} & h_{A21,MM} \end{bmatrix} - \begin{bmatrix} h_{A12,FF} & h_{A12,FM} \\ h_{A12,MF} & h_{A12,MM} \end{bmatrix} [H_2]^{-1} \begin{bmatrix} h_{A22,FF} & h_{A22,FM} \\ h_{A22,MF} & h_{A22,MM} \end{bmatrix}, \\
[H_{22}] &= \begin{bmatrix} h_{22,FF} & h_{22,FM} \\ h_{22,MF} & h_{22,MM} \end{bmatrix} \\
&= \begin{bmatrix} h_{A22,FF} & h_{A22,FM} \\ h_{A22,MF} & h_{A22,MM} \end{bmatrix} - \begin{bmatrix} h_{A22,FF} & h_{A22,FM} \\ h_{A22,MF} & h_{A22,MM} \end{bmatrix} [H_2]^{-1} \begin{bmatrix} h_{A22,FF} & h_{A22,FM} \\ h_{A22,MF} & h_{A22,MM} \end{bmatrix},
\end{aligned} \tag{2.55}$$

where

$$\begin{aligned}
[H_2]^{-1} &= \left\{ \begin{bmatrix} h_{A22,FF} & h_{A22,FM} \\ h_{A22,MF} & h_{A22,MM} \end{bmatrix} + \begin{bmatrix} h_{B22,FF} & h_{B22,FM} \\ h_{B22,MF} & h_{B22,MM} \end{bmatrix} \right\}^{-1} \\
&= \begin{bmatrix} h_{22,FF} & h_{2,FM} \\ h_{2,MF} & h_{2,MM} \end{bmatrix}^{-1}
\end{aligned} \tag{2.56}$$

Equations 2.55 and 2.56 yield 4 sets of non-linear equations which are solved to obtain FRFs of substructure B:

$$h_{B22,FF} = h_{2,FF} - h_{A22,FF}, \tag{2.57}$$

$$h_{B22,FM} = h_{B22,MF} = h_{2,FM} - h_{A22,FM}, \tag{2.58}$$

$$h_{B22,MM} = h_{2,MM} - h_{A22,MM}. \tag{2.59}$$

3 impact tests are conducted at points 1 and 2 to obtain the terms $h_{11,FF}$, $h_{12,FF}$ and $h_{22,FF}$, and the terms related to receptance at point A are calculated analytically. As a result, receptance matrix of point B which contains the spindle dynamics is shown below:

$$[H_{B,22}] = \begin{bmatrix} h_{B22,FF} & h_{B22,FM} \\ h_{B22,MF} & h_{B22,MM} \end{bmatrix} \tag{2.60}$$

After identifying the spindle dynamics, response of the spindle coupled with various holders can be predicted by using analytical model of the holder without further experimental measurements.

2.4 Construction of the Spindle-Holder-Extension-Tool Assembly by Receptance Coupling

A typical spindle-holder-extension and tool assembly is presented in Figure2.6.

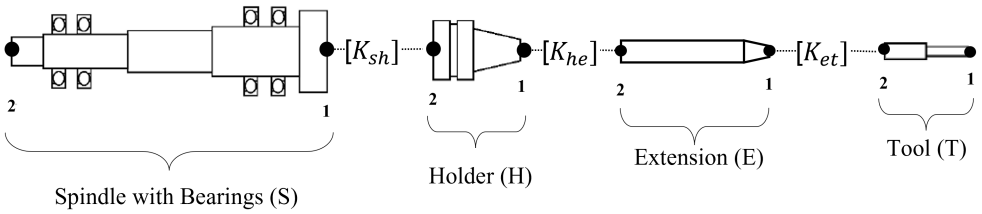


Figure 2.6: Spindle-holder-extension-tool Assembly

Once the dynamics of the spindle is identified and the end point receptance functions of the rest of the components are calculated, they can be coupled by including interface dynamics to obtain the response of the whole assembly. First, the end point receptance of the spindle is identified as described in Section 2.3. After calculating

the end point receptance of the holder, the receptance matrix of the spindle-holder at the holder tip point can be determined as [9]:

$$[SH_{11}] = [H_{11}] - [H_{12}].\left[[H_{22}] + [K_{sh}]^{-1} + [S_{11}]\right]^{-1}.[H_{21}] \tag{2.61}$$

where SH represents the spindle-holder sub-assembly, S represent the spindle and H represents the holder receptance. The complex stiffness representing the interface dynamics between the spindle and the holder is denoted by $[K_{sh}]$ [9]:

$$[K_{sh}] = \begin{bmatrix} k_y^{sh} + i.\omega.c_y^{sh} & 0 \\ 0 & k_\theta^{sh} + i.\omega.c_\theta^{sh} \end{bmatrix} \tag{2.62}$$

Here, k_y^{sh} and c_y^{sh} represent the translational stiffness and damping, k_y^{sh} and c_y^{sh} represent the rotational stiffness and damping, respectively.The receptance matrix of the extension can be coupled with the spindle-holder sub-assembly as follows:

$$[SHE_{11}] = [E_{11}] - [E_{12}].\left[[E_{22}] + [K_{he}]^{-1} + [SH_{11}]\right]^{-1}.[E_{21}] \tag{2.63}$$

where the direct and cross FRFs of the extension is denoted by $[E_{11}]$, $[E_{22}]$ and $[E_{12}]$, respectively. The interface dynamics between the holder and the extension is symbolized by $[K_{he}]$:

$$[K_{he}] = \begin{bmatrix} k_y^{he} + i.\omega.c_y^{he} & 0 \\ 0 & k_\theta^{he} + i.\omega.c_\theta^{he} \end{bmatrix} \tag{2.64}$$

Finally, tool should be coupled with the rest of the assembly to predict the tool tip FRF of the whole assembly.

$$[SHET_{11}] = [T_{11}] - [T_{12}].\left[[T_{22}] + [K_{et}]^{-1} + [SHE_{11}]\right]^{-1}.[T_{21}] \tag{2.65}$$

Similarly, the interface dynamics between the holder and the extension is symbolized by $[K_{et}]$:

$$[K_{et}] = \begin{bmatrix} k_y^{et} + i.\omega.c_y^{et} & 0 \\ 0 & k_\theta^{et} + i.\omega.c_\theta^{et} \end{bmatrix} \tag{2.66}$$

Note that the tool tip FRF matrix is in the following form

$$[SHET_{11}] = \begin{bmatrix} H_{11}^{SHET} & L_{11}^{SHET} \\ N_{11}^{SHET} & P_{11}^{SHET} \end{bmatrix} \tag{2.67}$$

Also notice that, the stability diagram is constructed by using the receptance function related to transverse displacement as a result of applied force which is H_{11}^{SHET}.

2.5 FRF Tuning Methodology

The aim of the chatter suppression at the tool tip is to increase the critical depth of cut. The stable depth of cut is negatively proportional to the negative real part of the tool tip FRF of the machine tool assembly as mentioned in the previous chapter [19]. Figure 2.7 depicts the SHET(spindle-holder-extension-tool) assembly as a combination of three substructures. The effective modes at the tip of the spindle-holder assembly should be identified in order to change the response of the assembly. By optimizing the dimensions of the extension and the tool, the match between the modes of the substructures therefore the absorber effect can be obtained. The opposite procedure in which geometric properties of the spindle-holder assembly are modified, can also be followed to achieve the dominant mode of the tool. In both cases, the dominant mode in the tool tip FRF divided into two smaller modes around the target mode.

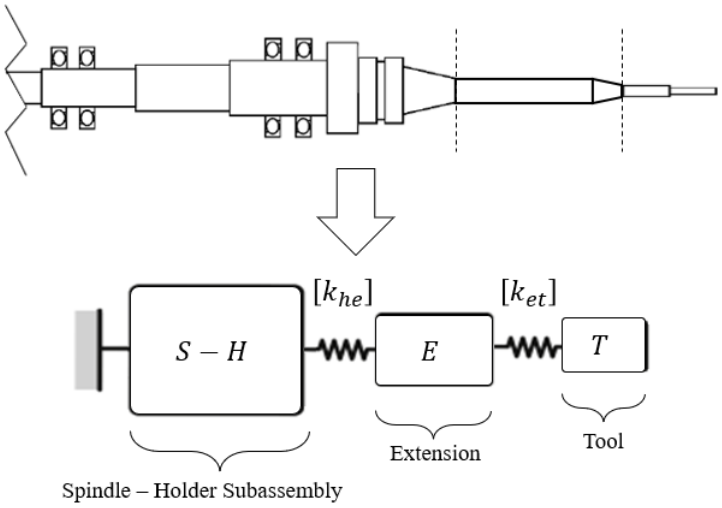


Figure 2.7: SHET assembly modeled as three substructures

In this thesis, optimal design parameters for extension-tool components are investigated for a specific range of frequency in order to attenuate the maximum amplitude

of the tool tip FRF. The objective function used for optimization can be expressed as:

$$\phi(x) = max\left(\left|H_{11}^{SHET}\right|\right) \tag{2.68}$$

$$x_{min} \leq x \leq x_{max}$$

Here, objective function is denoted by $\phi(x)$ and x represents the design parameters such as diameter and length of the extension. The optimization problem can be handled either for single variable or multiple variables such as; extension length and diameter, tool overhang length etc. can be evaluated simultaneously

CHAPTER 3

EXPERIMENTAL VERIFICATION

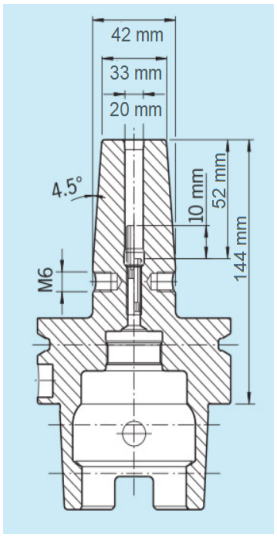
3.1 Introduction

In this chapter, experimental measurements conducted for identification of spindle dynamics and acquisition of FRFs of machine tool components is explained. First, machine tool components objected to impact tests are introduced. Then, experimental layout and data acquisition equipment are defined.Experimental procedure is explained and the comparison of experimental and predicted results are given.

3.2 Experimental Setup

In this section, experimental setup is explained and machine tool components are introduced. Impact hammer test is conducted under static conditions for four different experimental cases. Impact test is repeated for five times and the average of the five measurements is taken for each point of interest.

HAIMER holders are attached to the spindle of MAZAK VARIAXIS 630-5X CNC milling machine. First, HAIMER A63.144.20, which referred to as holder 1 in the following parts of the thesis, is inserted to the spindle. Figure 3.1 shows the dimensions and cross-section of the holder 1. Next, Holder 2 referred as to HAIMER A63.144.20.3 holder which is inserted to the spindle. Figure 3.2 shows the dimensions and cross-section of the holder 2. Dimensions of the holder 2 is almost the same as the holder 1 except the middle section of the holder 2 which has larger diameter.

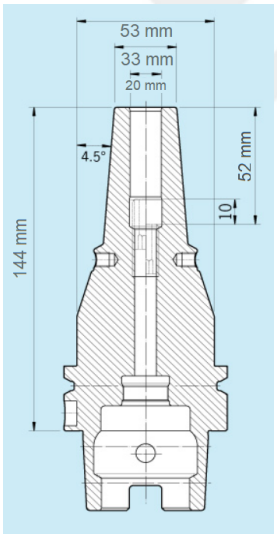


(a) Dimensions of HAIMER A63.144.20



(b) HAIMER A63.144.20

Figure 3.1: Technical Drawing and Photograph of Holder 1



(a) Dimensions of HAIMER A63.144.20.3



(b) HAIMER A63.144.20.3

Figure 3.2: Technical Drawing and Photograph of Holder 2

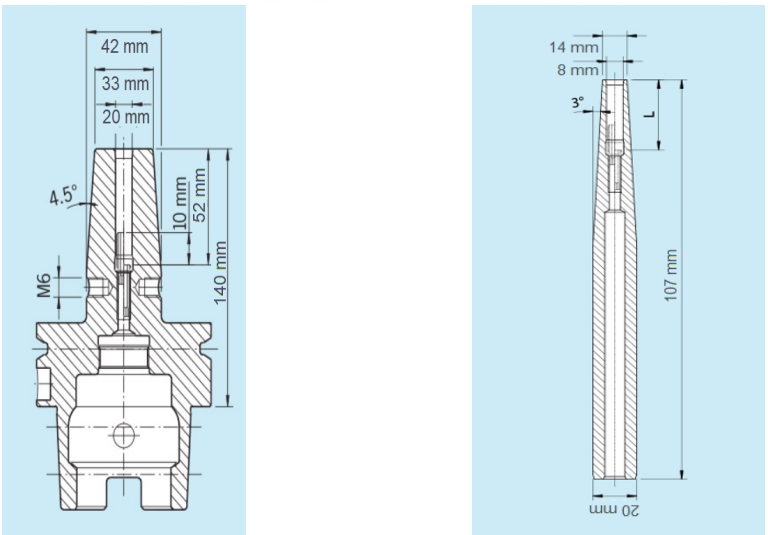
Then, HAIMER A63.140.20 referred as to holder 3 and the extension, which is inserted to holder 3 by shrink fit method, are mounted on the spindle. Dimensions of the holder 3 and the extension, and picture of the assembly is shown in Figure 3.4. As it

can be seen from the figures, all the holders and the extension have tapered geometry. Finally, M8 tool is inserted to the extension by shrink fit method and tool tip FRF is measured under static conditions.

Shrink fit method utilizes expansion and contraction of the components to be clamped in order to obtain interference fit. In thermal shrink fit, a joint between inner diameter of the extension and outer diameter of the tool is obtained by using heat. Figure 3.3 shows clamping a tool to a holder by thermal shrink fit method.



Figure 3.3: Shrink fit clamping between a holder and a tool



(a) Dimensions of HAIMER A63.140.20.3 (b) Extension

Figure 3.4: Technical Drawing and Photograph of Holder 3 and Extension



(c) HAIMER A63.140.20.3 and Extension Assembly

Figure 3.4: Technical Drawing and Photograph of Holder 3 and Extension

3.3 Impact Hammer Test and Measuring Equipment

Receptance functions of a system can be obtained by exciting the system at a single point and measuring the response from a single point. Impact hammer testing is one of the most commonly used method for measuring FRFs of a system. Excitation is provided by an impact hammer which is chosen considering the properties of the system. Accelerometers are widely used for measuring the response of the system. Impact hammer, accelerometer and data acquisition device used in the experiments are given in Figure 3.5 and CutPro software is used for processing the test data.



Figure 3.5: Measuring Equipment Used in Modal Testing

First, modal testing is condudted for HAIMER A63.144.20 holder. Accelerometer is mounted by wax on the measurement points. Both direct and cross FRFs are measured at point 1 and 2, additionally test procedure is repeated for x and y directions as shown in Figure 3.6.

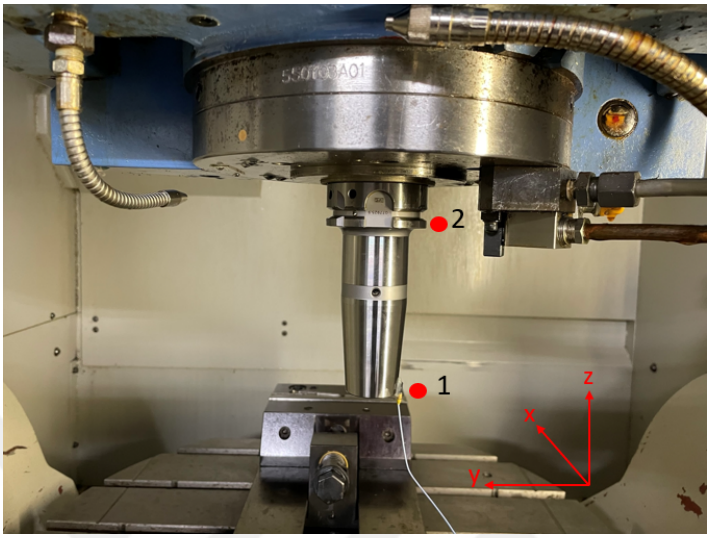


Figure 3.6: Experimental Setup of Holder 1

Second, FRF of HAIMER A63.144.20.3 holder is measured. The same experimental procedure is followed for holder 2 as in holder 1. Test layout is shown in Figure 3.7.

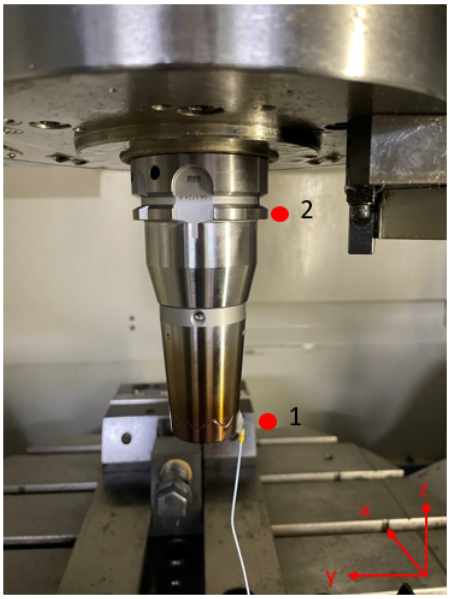
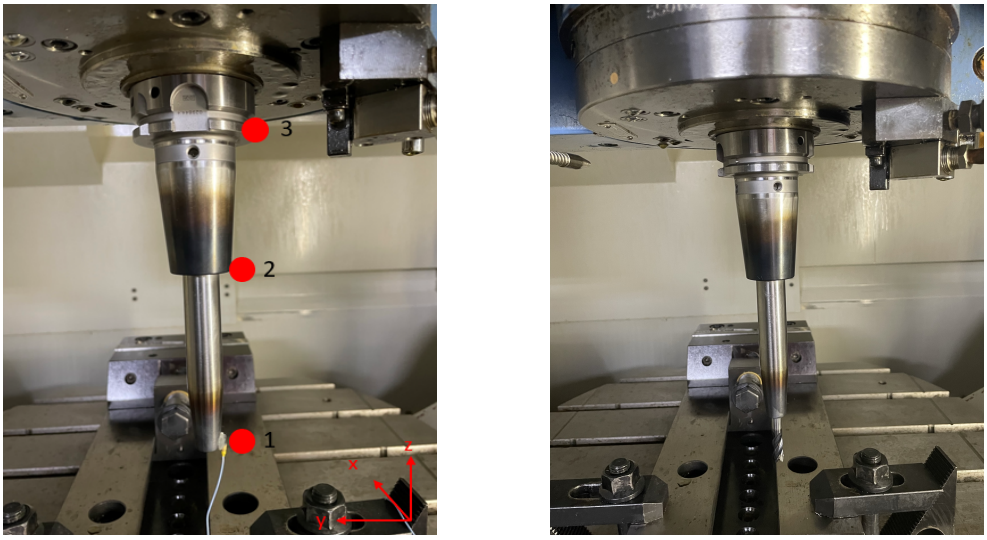


Figure 3.7: Experimental Setup of Holder 2

Then, FRF of the assembly of HAIMER A63.140.20 and extension component is measured. The same experimental procedure is followed for the assembly; however, additional measurement point, point 2, is added to be able to obtain the FRFs of the components separately. Point and transverse FRFs are measured for the test layout as shown in Figure 3.8a.

Finally, M8 tool with a length of 37.8 mm outside the holder is mounted into the extension by shrink fit method and the tool tip FRF of the SHET assembly is measured under static conditions as shown in Figure 3.8b.

Post-processing of the experimental data is done by using MATLAB to identify the response of the spindle based on receptance data. Verification of the identified spindle dynamics is done by coupling the analytically calculated receptance of the holders and comparing with the test data which is going to be explained in detail in the next section.



(a) Experimental Setup of Holder 3

(b) Experimental Setup with Tool

Figure 3.8: Experimental Setup of Holder 3, Extension and Tool

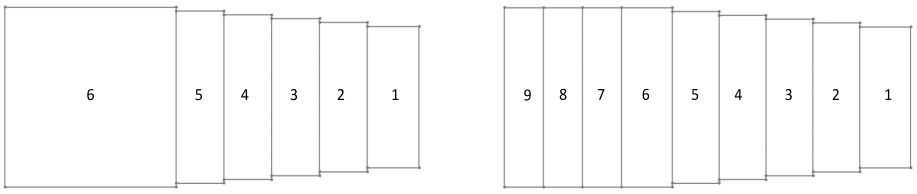
3.4 Experimental Results

In this section, experimental data processing procedure and experiment results are explained. First, dynamics of the spindle is identified at the spindle tip by using experimentally measured FRFs and inverse receptance coupling techniques as described in section. Second, identified spindle is coupled with analytically modeled holders, extension and a tool by receptance coupling method and compared with experimental results. Finally, effects of contact parameters are investigated.

3.4.1 Holder 1

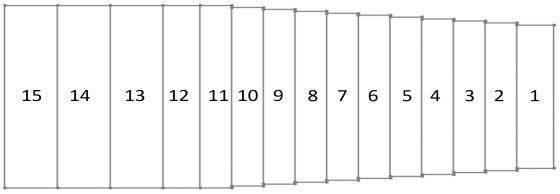
Dynamics of the spindle(receptance functions) are identified by subtracting analytically calculated receptance functions of the holders from experimentally measured FRFs of the spindle-holder assembly. Holders are divided into segments consist of cylindrical parts with various lengths and diameters. Response of the each segment is analytically calculated then coupled by receptance coupling method to obtain resultant response of the holder as a whole.

Holder 1 is divided into 6, 9 and 15 cylindrical segments as shown in Figure 3.9 in order to observe the effect of the number of segments on predicting the response of the part. Cylindrical segments used for modeling holder 1 is shown in Figure 3.9 and dimensions of the segments are given in Table 3.1. It is expected to have closer results to the test measurements as number of segments is increased.



(a) Holder 1 with 6 Segments (b) Holder 1 with 9 Segments

Figure 3.9: Holder 1 Modeled with Cylindrical Segments



(c) Holder 1 with 15 Segments

Figure 3.9: Holder 1 Modeled with Cylindrical Segments

Table 3.1: Dimensions of Holder 1 Segments

Segment Number	1	2	3	4	5	6
Length [mm]	13	12	12	12	12	43
Outer Diameter [mm]	33	35	36.5	38.5	40	42
Inner Diameter [mm]	20	20	20	20	20	0

(a) Dimensions of Holder 1 with 6 Segments

Segment Number	1	2	3	4	5	6	7	8	9
Length [mm]	13	12	12	12	12	13	10	10	10
Outer Diameter [mm]	33	35	36.5	38.5	40	42	42	42	42
Inner Diameter [mm]	20	20	20	20	0	0	0	0	0

(b) Dimensions of Holder 1 with 9 Segments

Segment Number	1	2	3	4	5	6	7	8	9	10
Length [mm]	7	6	6	6	6	6	6	6	6	6
Outer Diameter [mm]	33	34	35	36	36.5	37.5	38.5	39	40	41
Inner Diameter [mm]	20	20	20	20	20	20	20	20	0	0

(c) Dimensions of Holder 1 with 15 Segments

Segment Number	11	12	13	14	15
Length [mm]	6	7	10	10	10
Outer Diameter [mm]	42	42	42	42	42
Inner Diameter [mm]	0	0	0	0	0

(d) Dimensions of Holder 1 with 15 Segments Continued

Figure 3.10 shows the spindle tip FRF identified by subtracting analytically calculated receptance function of the holder 1 from experimentally measured FRFs of the spindle-holder 1 assembly. It is found that the most dominant mode is around 1500 Hz.

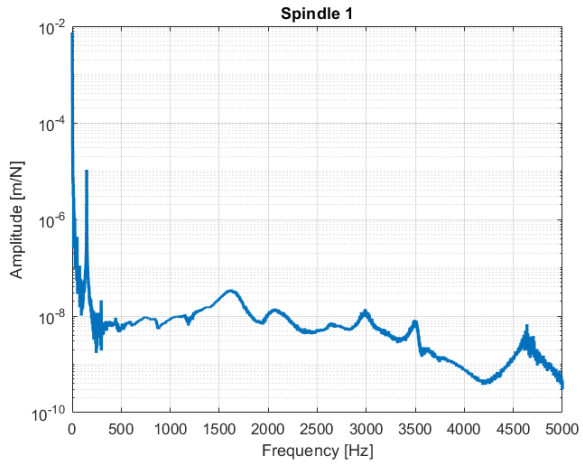
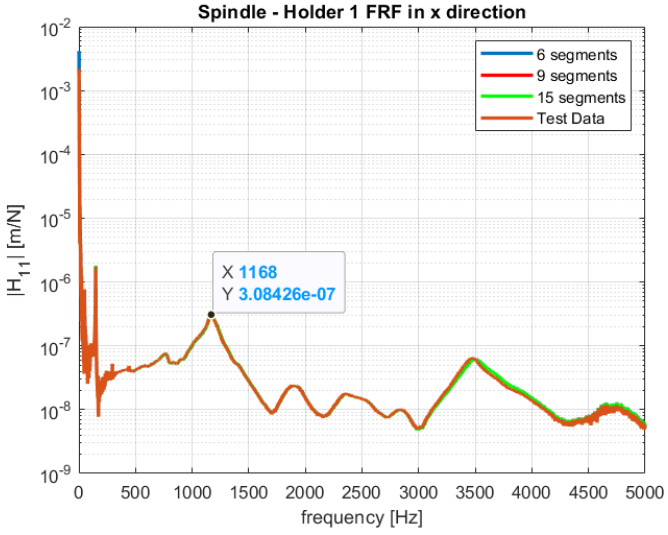


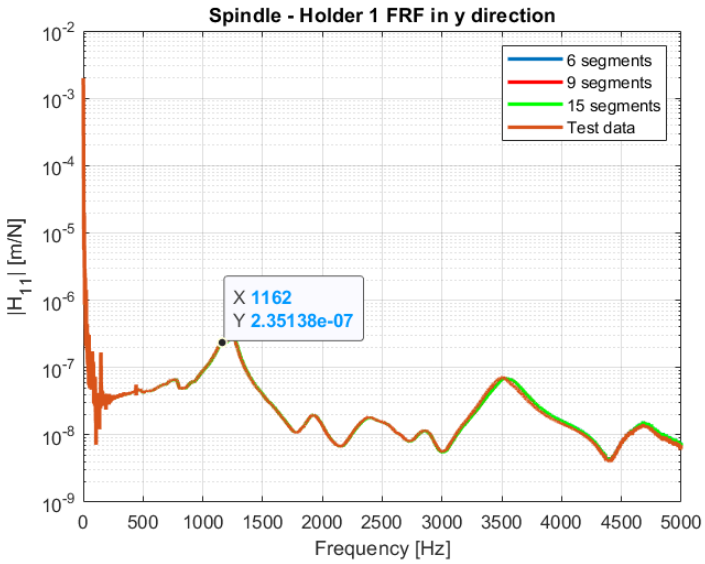
Figure 3.10: Identified Dynamics of Spindle by Using FRF Data of Holder 1

To verify the identification and coupling procedure, the same holder is re-coupled with the identified spindle. Figure 3.11 shows comparison of analytically predicted results and experimental data of holder 1 in both x and y directions.



(a) Calculated and predicted holder tip FRFs using different holder discretization in x direction

Figure 3.11: Spindle-Holder 1 FRF



(b) Calculated and predicted holder tip FRFs using different holder discretization in y direction

Figure 3.11: Spindle-Holder 1 FRF

It is seen that prediction and experiment results are in good agreement and increase in the number of segments does not significantly improves the response accuracy. Dominant mode is found to be around 1100-1200 Hz in both directions. Significant difference in response behavior is not observed between x and y directions.

3.4.2 Holder 2

To validate the spindle identification procedure, same identification procedure is applied using Holder 2 and spindle tip FRFs are identified. To do that, holder 2 is divided into 11 cylindrical segments which is shown in Figure 3.12 and dimensions of the segments are given in Table 3.2.

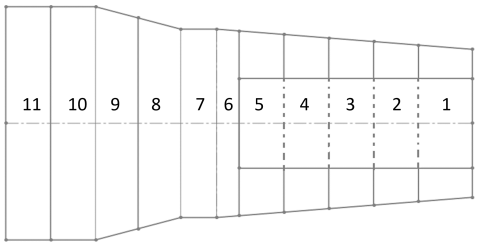


Figure 3.12: Holder 2 with 11 Segments

Table 3.2: Dimensions of Holder 2 Segments

Segment Number	1	2	3	4	5	6	7	8	9	10	11
Length [mm]	12	10	10	10	10	5	8	9.5	9.5	10	10
Outer Diameter [mm]	33	35	36.5	38	39.5	41	42	42	47	52	52
Inner Diameter [mm]	20	20	20	20	20	0	0	0	0	0	0

The same procedure as for holder 1 is followed for re-coupling the identified spindle with holder 2. Figure 3.13 shows the spindle tip FRF identified by subtracting analytically calculated receptance function of the holder 2. It is found that the most dominant mode is around 1600 Hz.

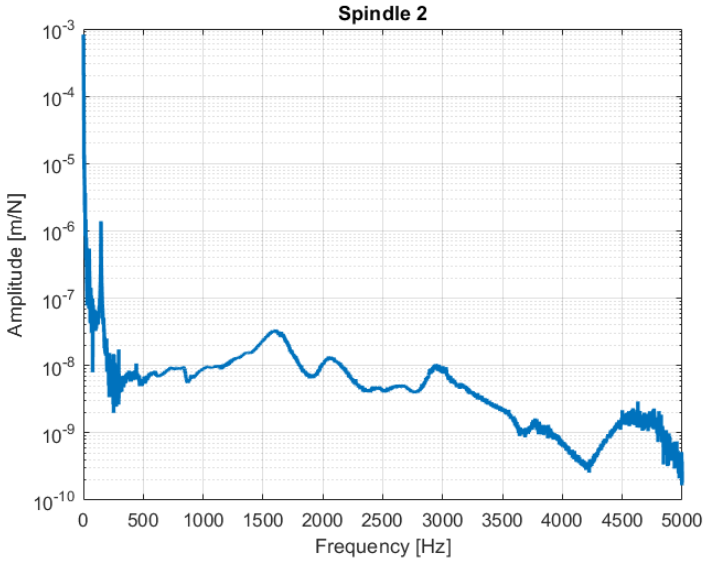
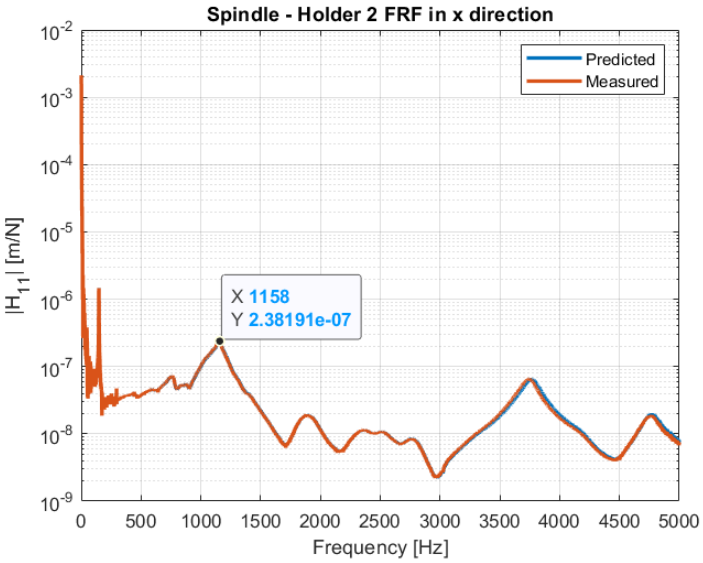
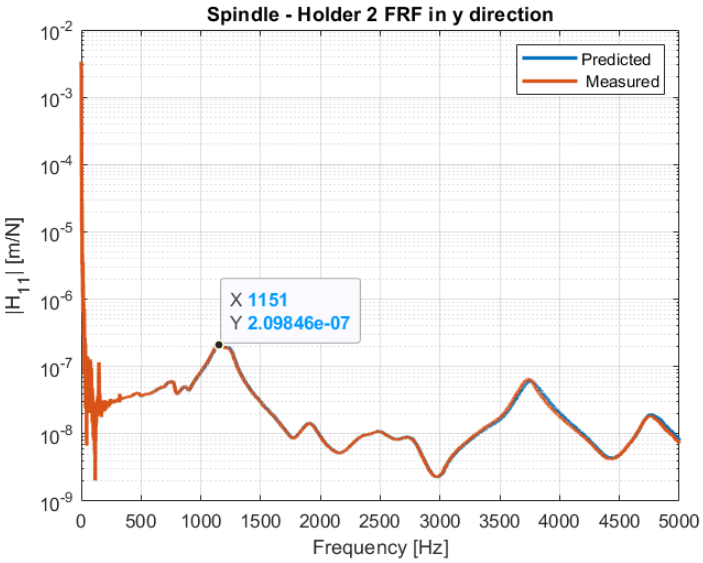


Figure 3.13: Identified Dynamics of Spindle by Using FRF Data of Holder 2

Figure 3.14 shows that the prediction of the response of holder 2 is consisted with the experimental data. Dominant frequency is found to be around 1100 Hz in both directions. Significant distinction is not observed between x and y directions.



(a) Calculated and predicted holder tip FRFs in x direction

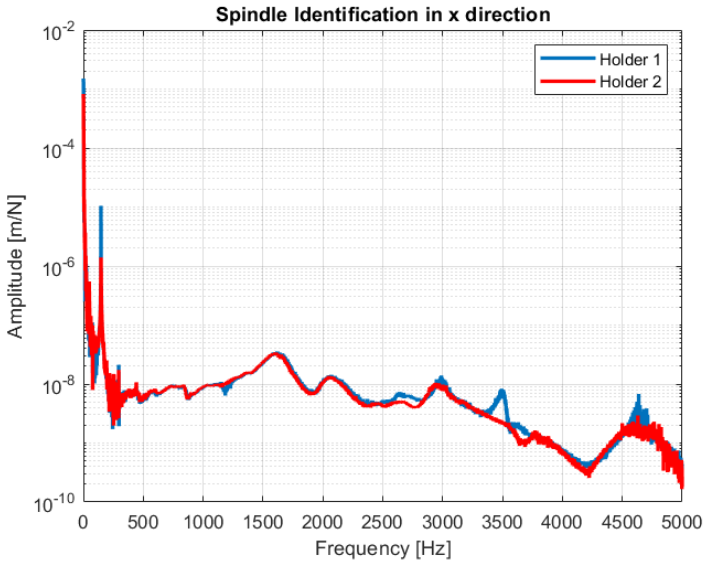


(b) Calculated and predicted holder tip FRFs in y direction

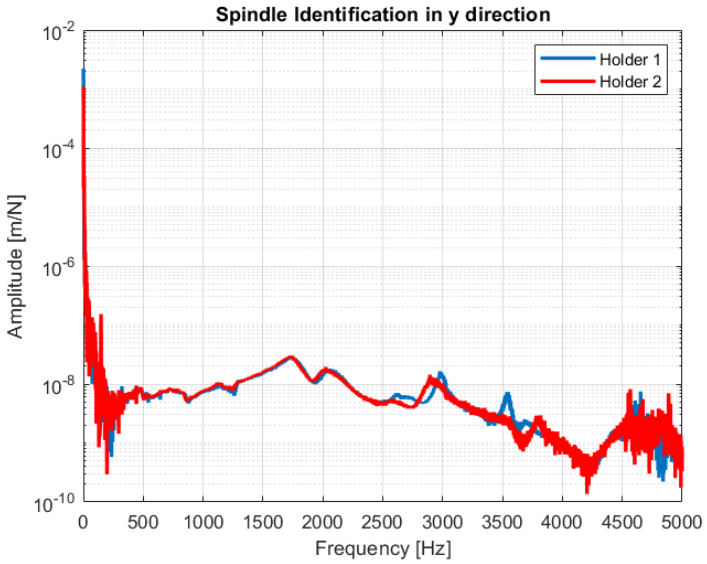
Figure 3.14: Spindle-Holder 2 FRF

It is expected that the response of the identified spindles by utilizing experimental

data of both holder 1 and holder 2 must be identical. Responses of the spindles are compared in each direction as shown in Figure 3.15. It is seen that responses are overlapping up to 2500 Hz. Even though there are minor differences after 2500 Hz, overall response of the spindle is consistent. It is seen that there is a dominant mode around 1600 Hz.



(a) Identified Spindle in x direction



(b) Identified Spindle in y direction

Figure 3.15: Identified Spindle FRFs

3.4.3 Holder 3 and Extension

Holder 3 and extension assembly is modeled with two different methods. First, holder and extension is assumed to be a single part where the contact at the holder-extension interface is assumed as rigid and divided into 18 segments shown as in Figure 3.16. Dimensions of each segment is given in Table 3.3.

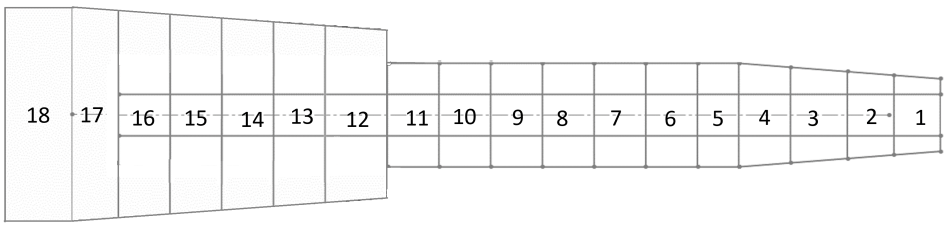


Figure 3.16: Holder 3 and Extension as a Unified Model

Table 3.3: Dimensions of Holder 3 Segments

Segment Number	1	2	3	4	5	6	7	8	9	10	11
Length [mm]	12	10	10	10	10	5	8	9.5	9.5	10	10
Outer Diameter [mm]	33	35	36.5	38	39.5	41	42	42	47	52	52
Inner Diameter [mm]	20	20	20	20	20	0	0	0	0	0	0

Table 3.3: Dimensions of Holder 3 Segments Continued

Segment Number	12	13	14	15	16	17	18
Length [mm]	12	10	10	10	10	5	8
Outer Diameter [mm]	33	35	36.5	38	39.5	41	42
Inner Diameter [mm]	20	20	20	20	20	0	0

In second method, holder and extension are modeled separately and analytically coupled with receptance coupling. Both cases of rigid contact and elastic contact between the holder and the extension are examined. Figure 3.17 shows analytically calculated FRF of holder 3 and extension assembly with free-free boundary conditions. It is

clear that both models can represent the assembly correctly. A set of elastic parameters at the junction point between holder 3 and extension are chosen to obtain FRF accurately which is given in Table 3.4. Slight change due to elastic contact between the holder and extension can be observed in Figure 3.17.

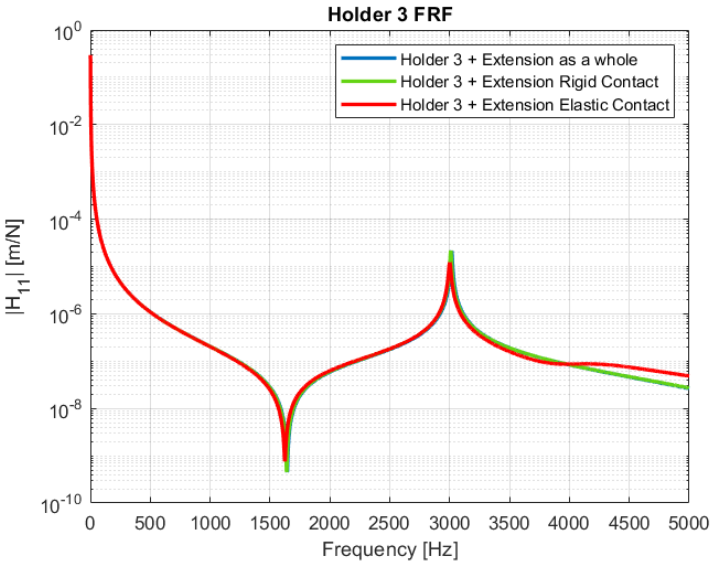
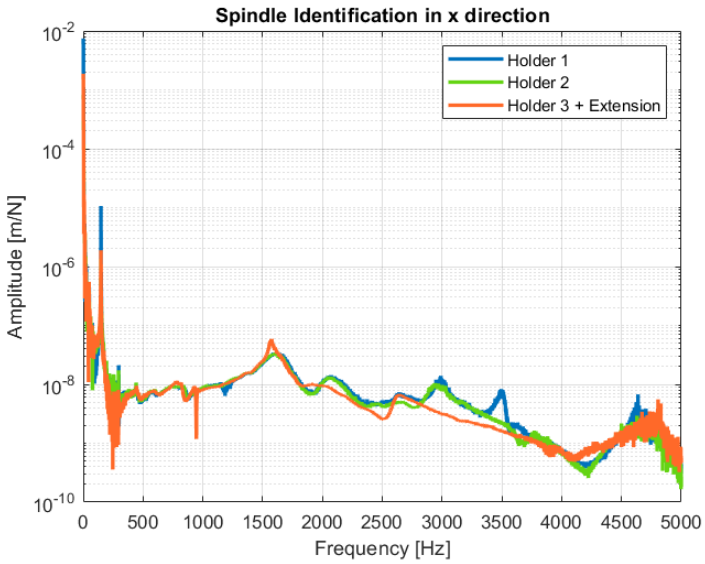


Figure 3.17: Holder 3 and Extension FRF with Free-Free Boundary Conditions

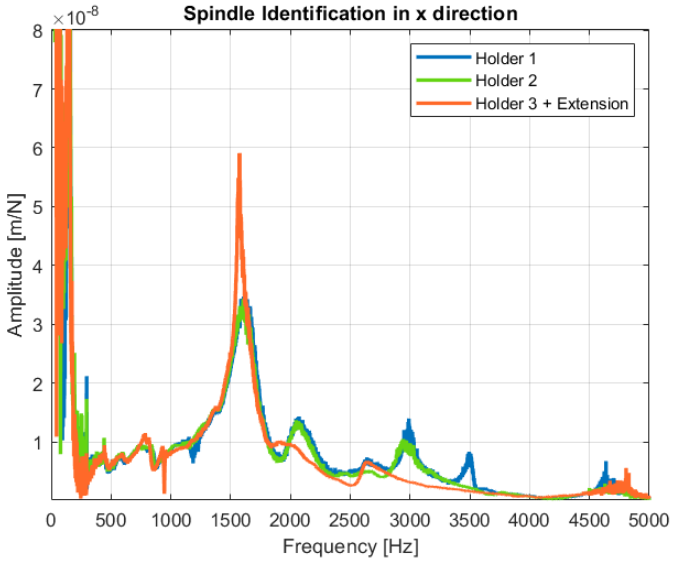
Table 3.4: Elastic Parameters of Holder 3 - Extension Assembly

Translational Stiffness [N/m]	3.10^{7}
Translational Damping [N.s/m]	300
Rotational Stiffness [N/rad]	7.10^{8}
Rotational Damping [N.s/rad]	170

Identified spindle which is obtained by experimental data of holder 3 and extension is compared with spindles identified by using holder 1 and holder 2 data. Although it is expected to have identical response from all spindles, it is shown that there is discrepancy around 1600 Hz and in regions where frequency is higher than 2000 Hz as shown in Figure 3.18.



(a) Identified Spindles in Logarithmic Scale



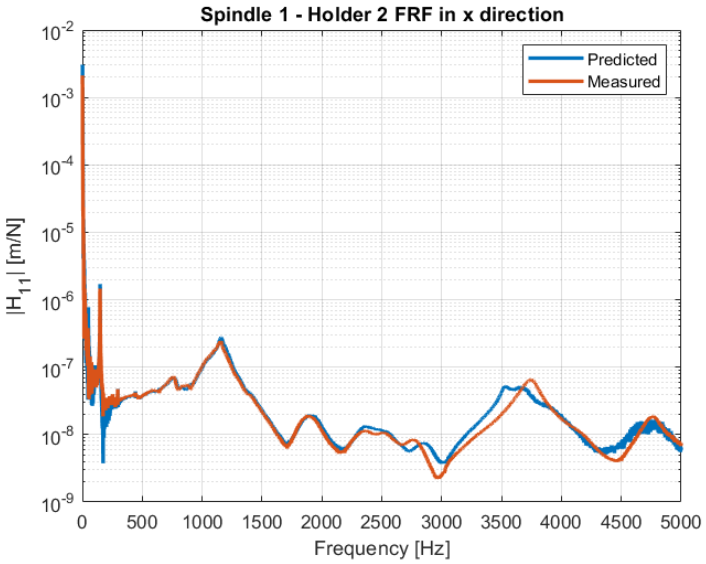
(b) Identified Spindles in Linear Scale

Figure 3.18: Comparison of Identified Spindles

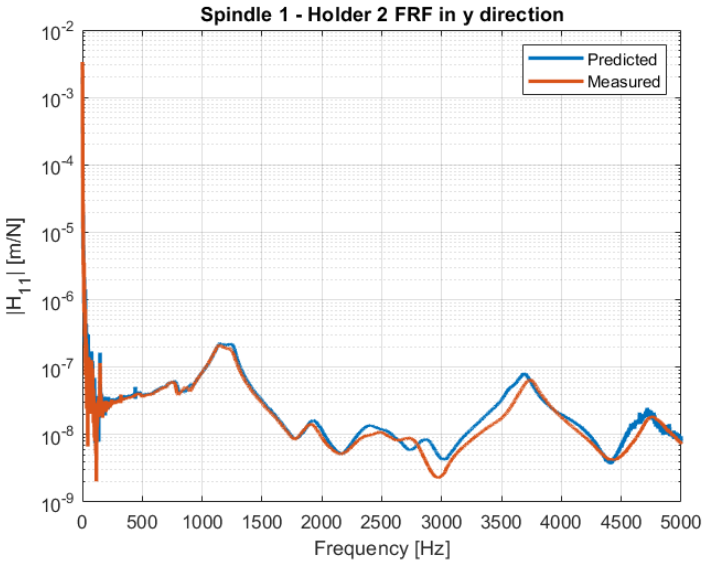
3.4.4 Prediction of Holder-Extension Tip FRFs Using Identified Spindles

Identified spindle using experimental data of holder 1 is analytically coupled with holder 2 and compared with the experiment results as shown in Figure 3.19. It can

be deduced from the figures that the spindle dynamics are identified with a good accuracy, independent of which holder is used for the identification. It is guessed that the discrepancy occurring after 2500 Hz is due to the holder modes. Significant difference is not observed between x and y directions.



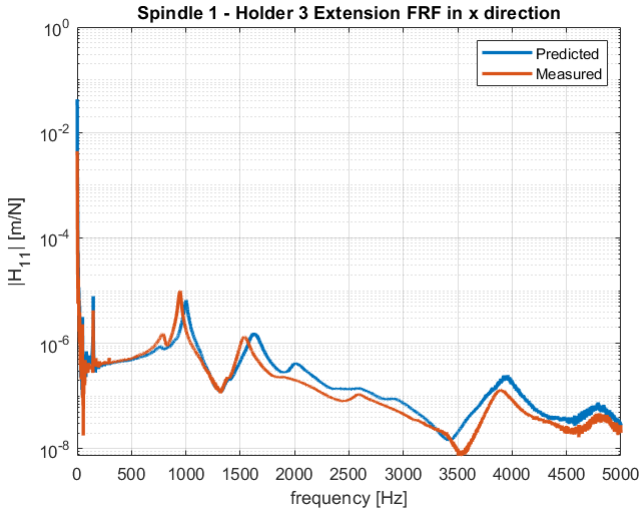
(a) Spindle Identified Using Holder 1 Coupled with Holder 2 FRF in x direction



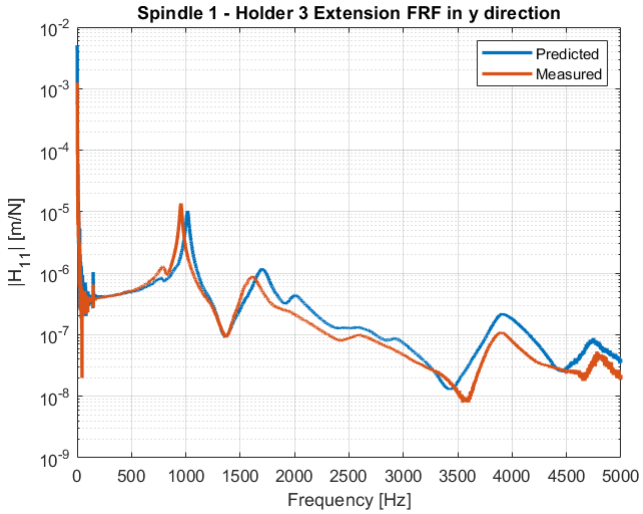
(b) Spindle Identified Using Holder 1 Coupled with Holder 2 FRF in y direction

Figure 3.19: Spindle Identified Using Holder 1 Coupled with Holder 2 FRF

Analytically calculated receptance of the holder 3 - extension assembly is also coupled with aforementioned spindle and compared with the test results as shown in Figure 3.20. All contacts between the components are modeled as rigid. The difference between experiment results and predicted FRFs is greater for the holder 3-extension assembly, compared to holder 2, furthermore; in high frequency region, the gap between two plots is increased.



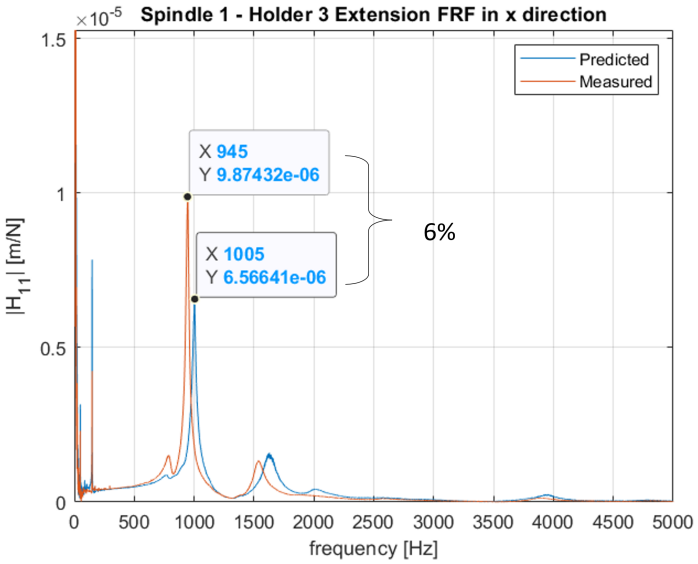
(a) Spindle Identified Using Holder 1 Coupled with Holder 3 FRF in x direction



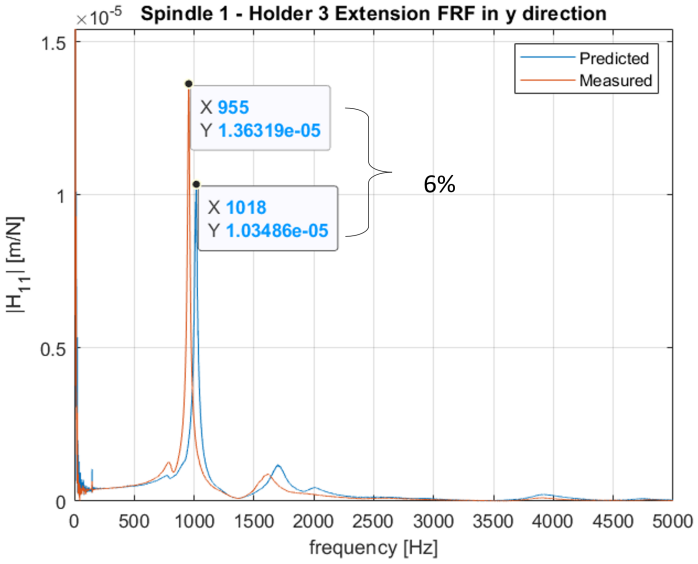
(b) Spindle Identified Using Holder 1 Coupled with Holder 3 FRF in y direction

Figure 3.20: Spindle Identified Using Holder 1 Coupled with Holder 3 FRF

However, it is seen that the amplitudes of the high frequency modes are considerably small with respect to mode around 950 Hz in linear scale as shown in Figure 3.21. The difference between experimental results and predicted values are 6% which is not significantly high.



(a) Spindle Identified Using Holder 1 Coupled with Holder 3 FRF in x direction



(b) Spindle Identified Using Holder 1 Coupled with Holder 3 FRF in y direction

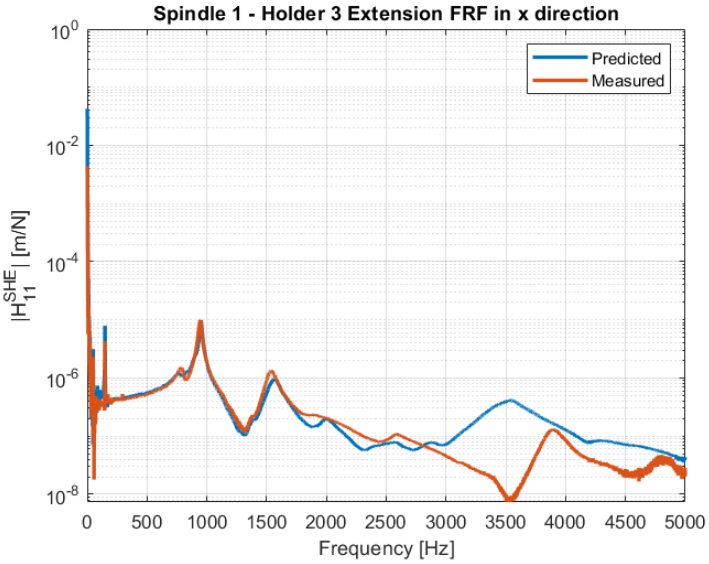
Figure 3.21: Spindle Identified Using Holder 1 Coupled with Holder 3 FRF in Linear Scale

Elastic contact between the holder and extension is defined in order to have agreement between the prediction and measurement data. Table 3.4 shows the identified values of elastic contact parameters between the holder and extension.

Table 3.4: Elastic Parameters of Holder 3 - Extension Assembly for Spindle 1 - Holder 3 - Extension Coupling

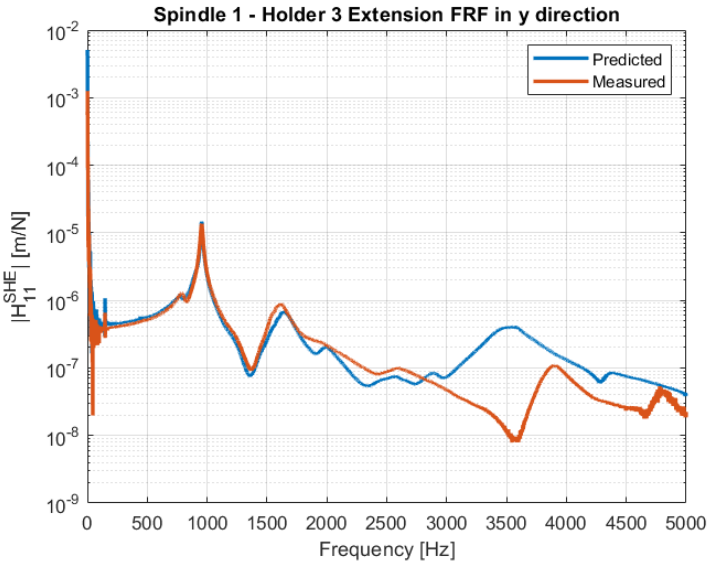
Translational Stiffness [N/m]	4.10^7
Translational Damping [N.s/m]	3000
Rotational Stiffness [N/rad]	7.10^8
Rotational Damping [N.s/rad]	170

The improving effect of the addition of the elastic contact on the extension tip FRF is shown in Figure 3.22. Even though rigid contact between spindle 1 and holder 3 is preserved, 6% difference between the prediction and measurement is almost eliminated when a contact parameter is defined between the holder and extension.



(a) Spindle Identified Using Holder 1 Coupled with Holder 3-Extension FRF in x direction(Elastic Contact Between Holder 3-Extension)

Figure 3.22: Spindle Identified Using Holder 1 Coupled with Holder 3-Extension FRF (Elastic Contact Between Holder 3-Extension)



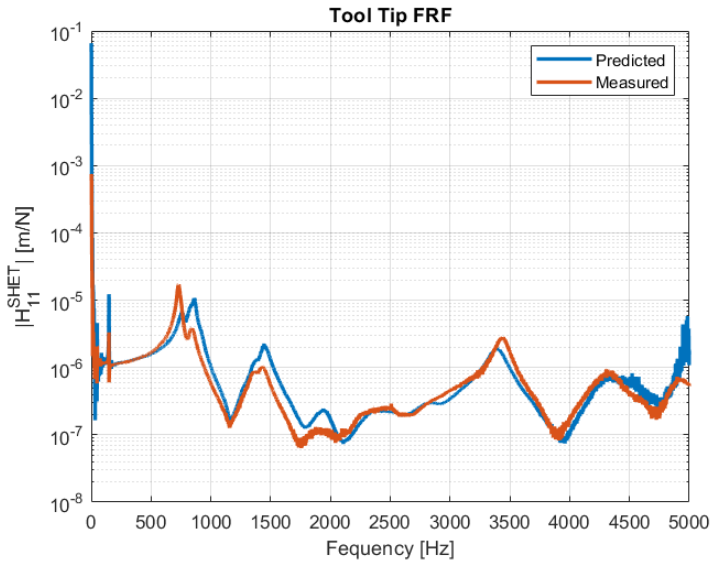
(b) Spindle Identified Using Holder 1 Coupled with Holder 3-Extension FRF in y direction(Elastic Contact Between Holder 3-Extension)

Figure 3.22: Spindle Identified Using Holder 1 Coupled with Holder 3-Extension FRF (Elastic Contact Between Holder 3-Extension)

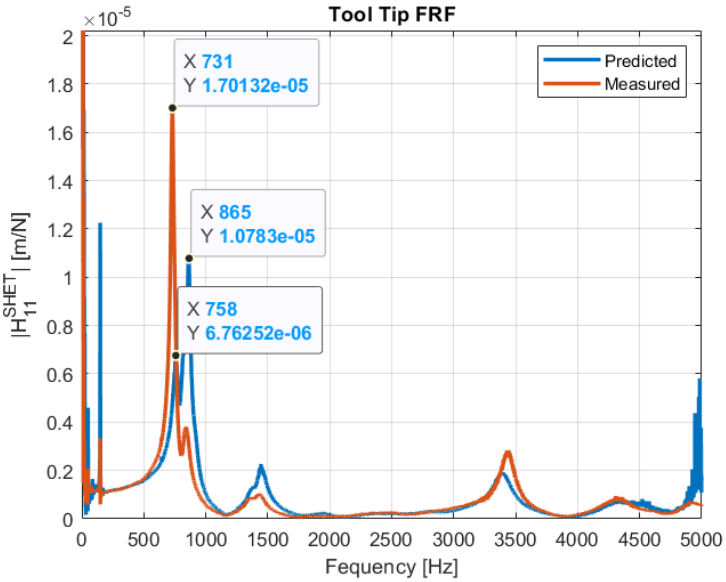
3.4.5 Holder 3-Extension and Tool

8M tool is inserted into the extension part by thermal shrink fit as shown in Figure 3.8b and impact test is conducted to obtain tool tip FRF under static conditions. Identified spindle by using response of holder 1 is analytically coupled with the holder 3-extension and tool assembly and comparison of the predicted and measured FRFs are given in Figure 3.23.

All of the contacts between the components are modeled as rigid therefore sufficient agreement between the predicted and experimental data is not achieved. The dominant mode is found to be at 731 Hz which can be seen when results are plotted in linear scale.



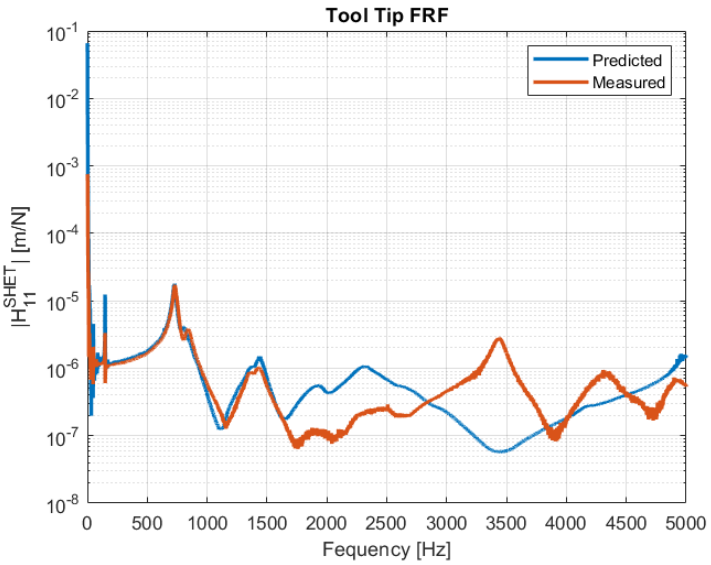
(a) Tool Tip FRF



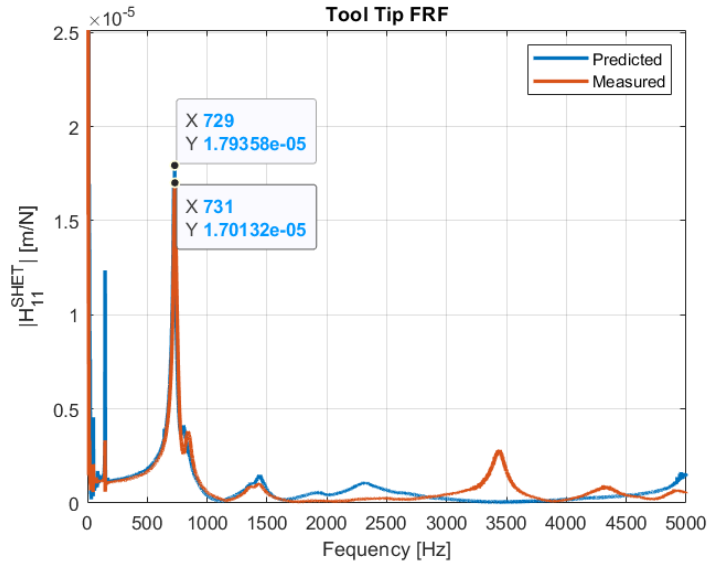
(b) Tool Tip FRF in Linear Scale

Figure 3.23: Tool Tip FRF

The consistency between the test results and analytical model can be achieved by including the elastic contact effect. The mode at 731 Hz is the focus point where overlap is desired since it dominates the response of the system. Figure 3.24 shows the improving effect of adding elastic contact between holder and the extension on tool tip FRF.



(a) Tool Tip FRF with Elastic Contact Between Holder and Extension



(b) Tool Tip FRF with Elastic Contact Between Holder and Extension Linear Scale

Figure 3.24: Tool Tip FRF with Elastic Contact Between Holder and Extension

Table 3.5 gives the elastic parameters chosen to obtain the desired agreement between experimental results and predicted values. The error value is reduced from 3% to 0.3%, resulting in a tenfold improvement in results. In addition to elastic contact at the junction of holder and extension, the contact between the extension and the tool is also defined as elastic.

Table 3.5: Elastic Parameters Between Holder 3 - Extension Assembly

Translational Stiffness [N/m]	3.10^7
Translational Damping [N.s/m]	300
Rotational Stiffness [N/rad]	7.10^8
Rotational Damping [N.s/rad]	170

CHAPTER 4

SENSITIVITY ANALYSIS IN SPINDLE - HOLDER - EXTENSION - TOOL ASSEMBLY

In this chapter, the effects of the geometric properties of the holder-extension-tool sub-assembly on the tool tip FRF are investigated. As mentioned in Chapter 2, mode interaction between the components of the machine tool assembly can suppress the chatter vibration due to absorber effect. Therefore, investigation of the design parameters effect on the chatter suppression by tuning methodology has a great importance.

4.1 Investigation of the Effects of the Interface Dynamics

In this section, effects of the contact between the holder-extension and the extension-tool depending on the interface length is investigated through simulations. The machine tool assembly considered in this section is shown in Figure 3.8b. Contacts between the components are modeled as elastic and values are identified by following the procedure given in Chapter 3.

4.1.1 Effect of Holder-Extension Interface Dynamics

Contact parameters between the holder-extension and extension-tool are identified by using experimentally measured spindle-holder 3-extension tip FRF data and analytical model of holder 3-extension as in methodology followed in Chapter 3. Identified stiffness and damping values in both translational and rotational directions for holder 3-extension and extension-tool are given in Table 4.1 and Table 4.2, respectively. Effects of the contact area between the components are investigated while the identified contact parameters are remained unchanged for all the cases.

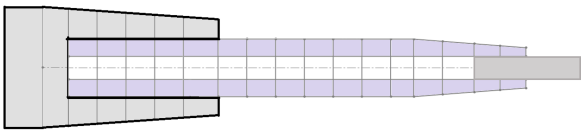
Table 4.1: Identified Elastic Parameters Between Holder 3 - Extension

Translational Stiffness [N/m]	4.10^7
Translational Damping [N.s/m]	3000
Rotational Stiffness [N/rad]	7.10^8
Rotational Damping [N.s/rad]	170

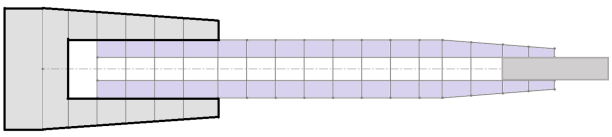
Table 4.2: Identified Elastic Parameters Between Extension - Tool

Translational Stiffness [N/m]	7.10^7
Translational Damping [N.s/m]	700
Rotational Stiffness [N/rad]	$1.5.10^8$
Rotational Damping [N.s/rad]	100

First, holder 3-extension assembly is modeled such that extension is inserted into holder 3 without a space as shown in Figure 4.1a. Then, the extension is moved outside of the holder 3 with 10 mm increments as shown in Figure 4.1b and Figure 4.1c. Position of the tool inside the extension is remained unchanged for all the cases.

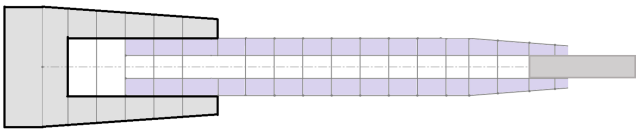


(a) Holder 3-Extension Contact Interface at Initial Position



(b) Holder 3-Extension Contact Interface Length Decreased 10 mm

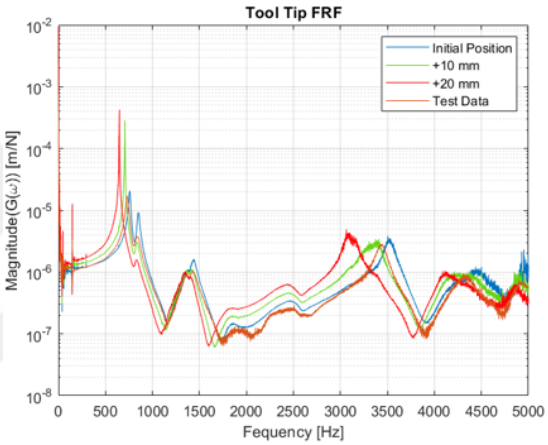
Figure 4.1: Change of Holder 3-Extension Contact Interface Length



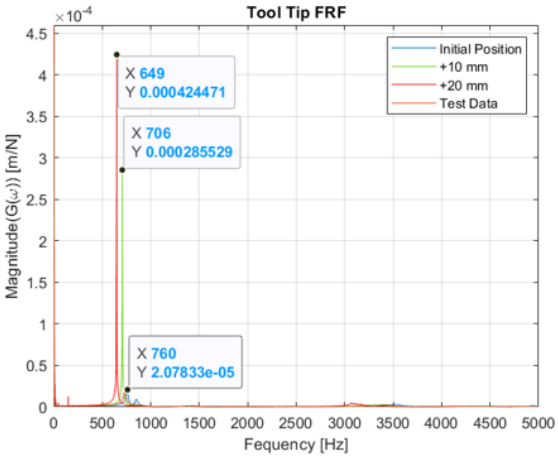
(c) Holder 3-Extension Contact Interface Length Decreased 20 mm

Figure 4.1: Change of Holder 3-Extension Contact Interface Length - Continued

Effects of the contact length at the interface of the holder 3-extension on tool tip FRF is analytically calculated and compared with the experiment data as shown in 4.2.



(a) Effect of Holder 3-Extension Contact Interface Length on Tool Tip FRF in Logarithmic Scale



(b) Effect of Holder 3-Extension Contact Interface Length on Tool Tip FRF in Linear Scale

Figure 4.2: Effect of Holder 3-Extension Contact Interface Length on Tool Tip FRF

As shown in Figure 4.2a, the most flexible mode moved from 760 Hz to 650 Hz as the length of the interface is decreased. As extension is moved 10 mm outside of the holder, amplitude of the most flexible mode is increased about 90% which indicates decrease in rigidity as expected. It is observed that the contact between the holder 3-extension significantly affects the dominant mode of the tool tip FRF.

4.1.2 Effect of Extension-Tool Interface Dynamics

The effect of the contact interface length between the extension and tool is investigated in this section. Elastic contact parameters given in Table 4.1 and Table 4.2 is remained unchanged and extension is fully inserted into the holder 3. Tool length inside the extension is increased by 8 mm increments as shown in Figure 4.3.

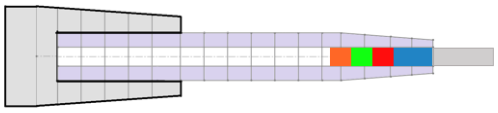
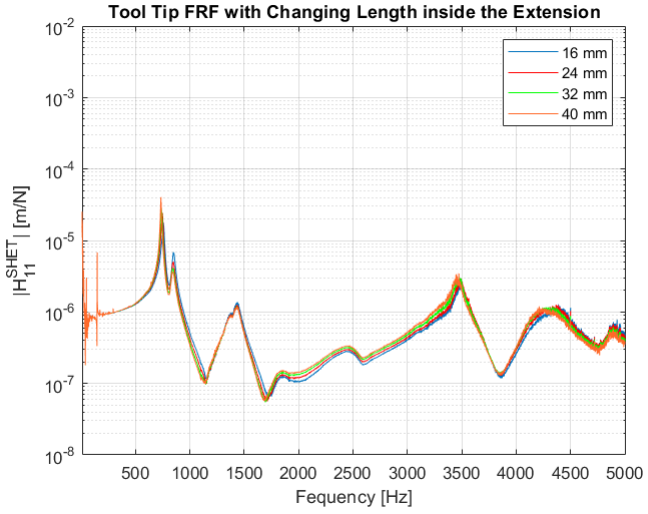
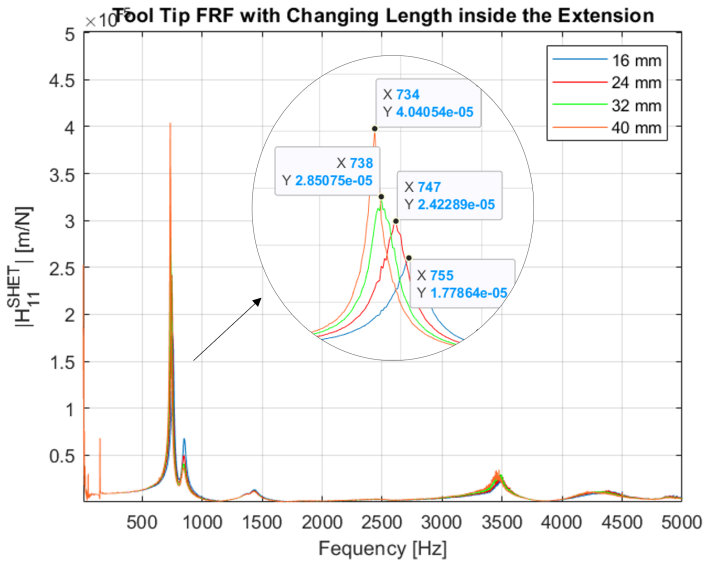


Figure 4.3: Incremental Tool Length Increase inside the Extension

Effects of incremental increase of tool length inside the extension on tool tip FRF is shown in Figure 4.4.



(a) Effect of Extension-Tool Contact Interface Length on Tool Tip FRF in Logarithmic Scale



(b) Effect of Extension-Tool Contact Interface Length on Tool Tip FRF in Linear Scale

Figure 4.4: Effect of Extension-Tool Contact Interface Length on Tool Tip FRF

It can be seen that as length of the tool inside the extension is increased, the dominant mode moves from 755 Hz to 735 Hz and the amplitude is increased as shown in Figure 4.4b. However, it is observed that increasing the tool length inside the extension does not significantly effects the dominant mode when compared to change of interface length of the holder 3-extension.

4.2 Effect of the Change of Extension Diameter

In this section, effect of the geometric properties on tool tip FRF is investigated. Various extension profiles with increased diameters are examined. Contact parameters are preserved since the geometry and position of the extension inside the holder is not change while extension geometry outside the holder is modified.

4.2.1 Diameter Increase of Segments 10 and 11

Segments 11 and 10 are the closest segments to the holder at the outside of the holder as shown in Figure 4.5. Contacts between the holder 3-extension and extension-tool

is modeled as elastically and elastic contact parameter values are the same as in Table 4.1 and Table 4.2, respectively.

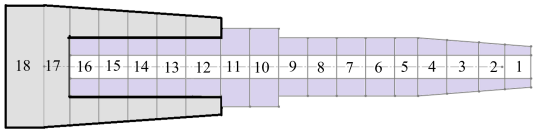


Figure 4.5: Segments of the Extension with Increased Diameter

The length of extension outside the holder is 107 mm and tool length outside the extension is 37.8 mm. While investigating the effect of the diameter on tool tip FRF, lengths of the extension and tool is remained unchanged. Figure 4.6 shows calculated tool tip FRF through simulations with various diameters.

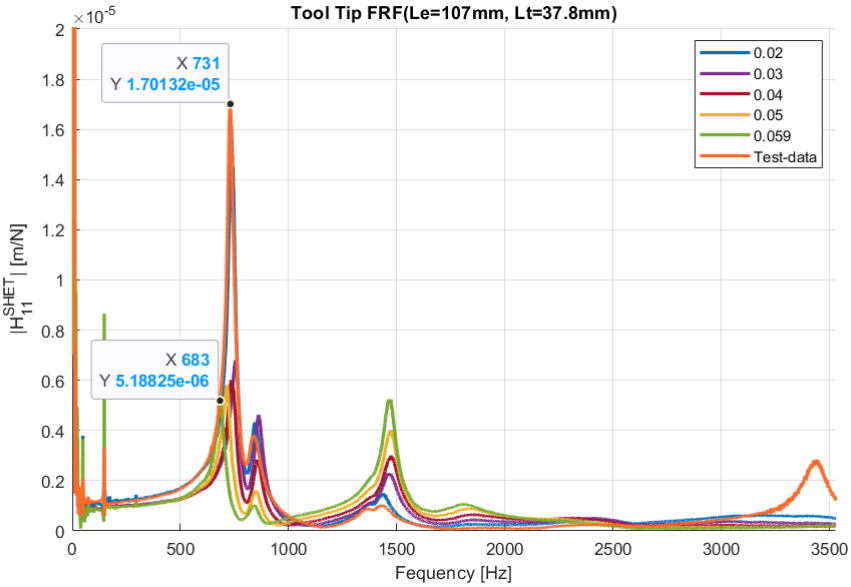


Figure 4.6: Tool Tip FRF with Increased Diameter of Segments 10 and 11

As the diameter of segments is increased, the dominant mode shifts from 731 Hz to 683 Hz and 68% decrease in amplitude is achieved. It is expected to have smaller amplitudes and lower frequencies since diameter increase leads to stiffer extension structure. Figure 4.7 shows the maximum amplitude of tool tip FRF with respect to extension diameter between 600-800 Hz where he most flexible mode is located.

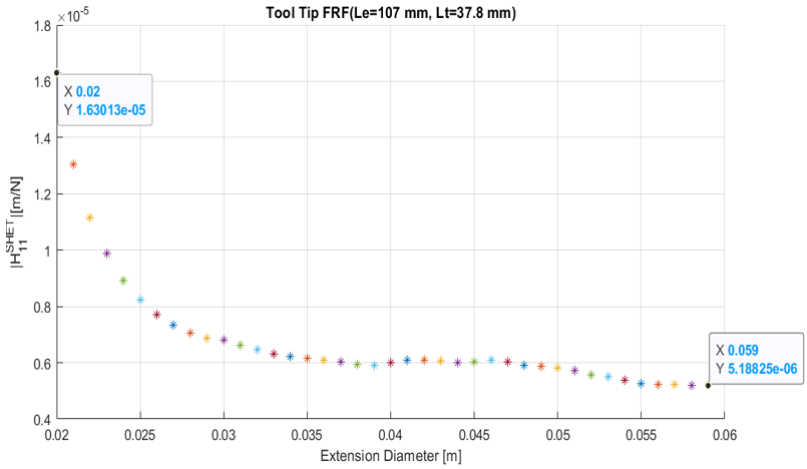


Figure 4.7: Maximum Tool Tip FRF Amplitude with Changing Segment Diameter

Dramatic decreasing trend in the amplitude of tool tip FRF is observed between 20 mm and 35 mm. The amplitude remains almost steady after 35 mm which indicates that further increase in diameter does not provide effective attenuation.

The effect of the diameter change of the segments 10 and 11 on the cutting stability is investigated through simulations using CutPro software. Figure 4.8 shows the comparison of the SLD calculated by using measured FRF data for holder 3-extension-tool assembly and analytical model of the same assembly with 60 mm diameter of the extension segments 10 and 11. Tool with 4 flutes and 8 mm diameter is used for slotting operation of a rigid Aluminum 7050 workpiece for SLD calculations.

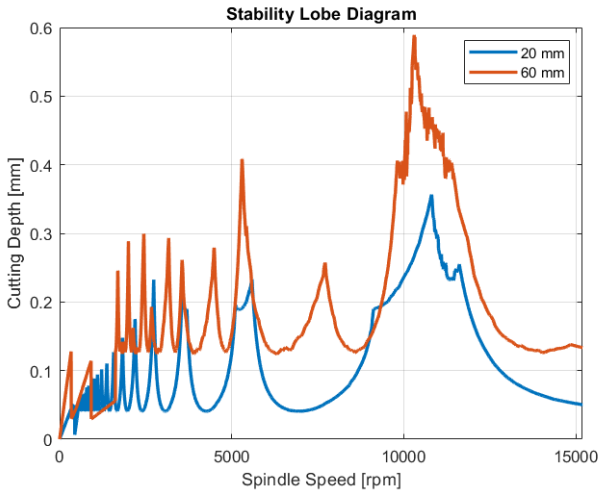


Figure 4.8: Comparison of Stability Lobe Diagrams for Initial Geometry of Extension and Increased Diameter of the Segments 10 and 11 to 60 mm

It is shown that average critical depth of cut is almost tripled as a result of diameter increase which is consistent with the tool tip FRFs. The critical depth of cut is significantly increased from 0.05 mm to 2.5 mm between 6000-8000 rpm.

4.2.2 Diameter Increase of Segments 8 and 9

Diameter of the segments located in the middle section of the extension is increased as shown in Figure 4.9. The same procedures is followed for the simulations as in the previous section.

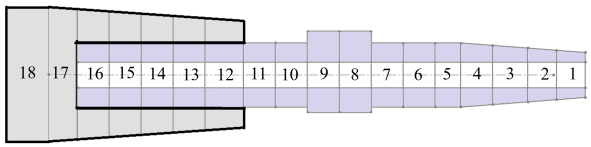


Figure 4.9: Segments of the Extension with Increased Diameter

Effect of the diameter change in the middle section of the extension on the tool tip FRF is shown in Figure 4.10. Attenuation effect at the dominant mode due to increased diameter is also observed however, shift of the dominant mode is spread in a wider region compared to Figure 4.6.

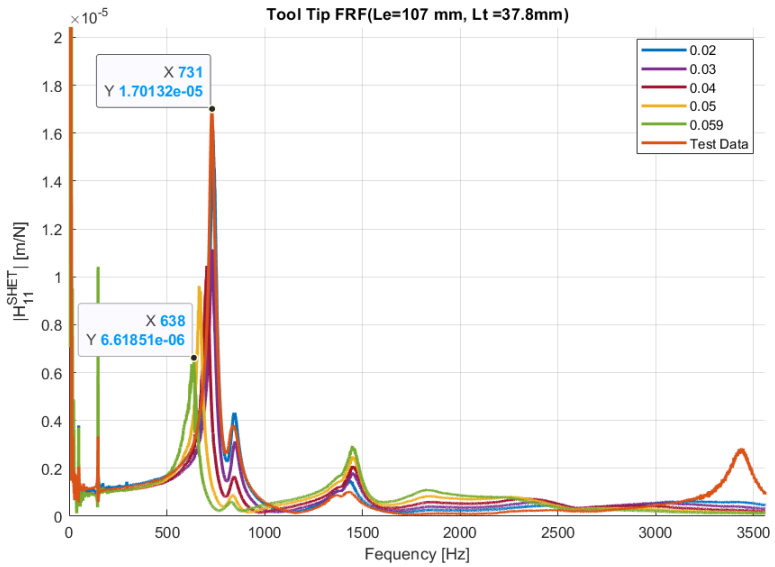


Figure 4.10: Tool Tip FRF with Increased Diameter of Segments 8 and 9

Figure 4.11 shows the maximum tool tip FRF with changing segment diameter from 20 mm to 60 mm with 1 mm increments. Maximum tool tip amplitude is decreased rapidly between 20 mm and 25 mm. Steady decline is observed between 25 mm and 50 mm and gradual decrease continues after 50 mm. Almost 60% decrease in the maximum tool tip amplitude is achieved in 600-800 Hz range.

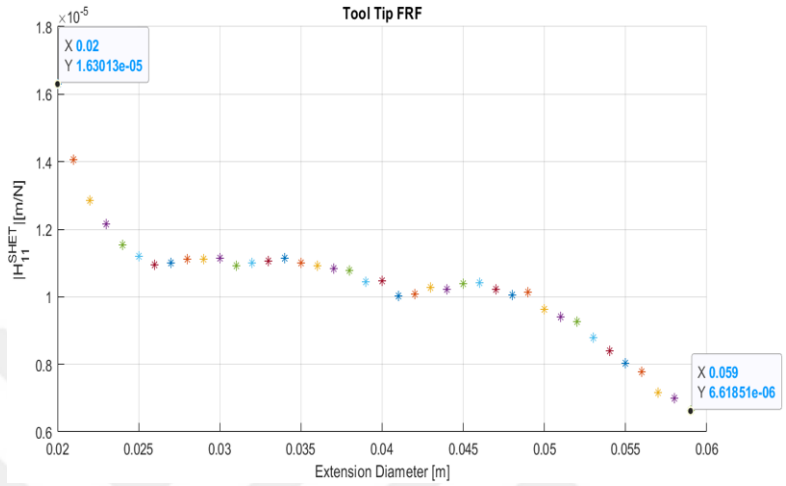


Figure 4.11: Maximum Tool Tip FRF Amplitude with Changing Segment Diameter

The same procedure is followed for this case to calculate SLDs. Figure 4.12 shows the comparison of the SLD calculated by using measured FRF data for holder 3-extension-tool assembly and analytical model of the same assembly with 60 mm diameter of the extension segments 8 and 9.

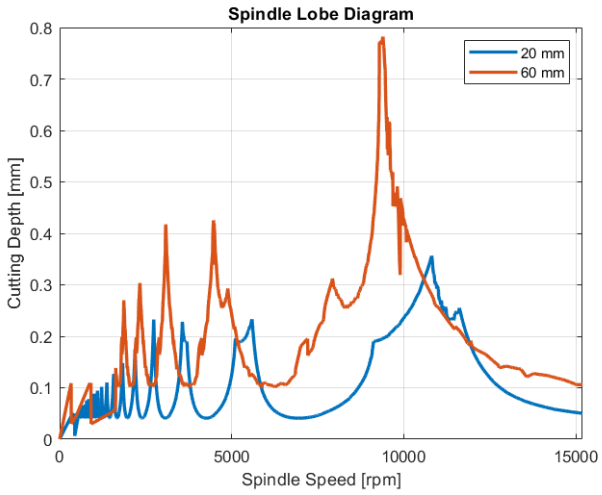


Figure 4.12: Comparison of Stability Lobe Diagrams for Initial Geometry of Extension and Increased Diameter of the Segments 8 and 9 to 60 mm

It is shown that as the diameter of the segments 8 and 9 is increased to 60 mm which provides the minimum tool tip FRF amplitude, the stable cutting region is increased. Significant improvement in chatter free depth of cut is obtained around 4000 rpm and between 7000-10000 rpm. It can be concluded that as the segments with larger diameter is moved to the tip of the extension,improvement on the SLD is decreases when compared to Figure 4.8.

4.2.3 Diameter Increase of Segments 6 and 7

Segments 6 and 7 are located close to the tip of the extension as shown in Figure 4.13.

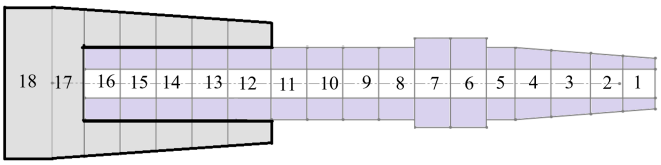


Figure 4.13: Segments of the Extension with Increased Diameter

Tool tip FRF of the SHET assembly with increased diameters at the extension tip is calculated through simulations and results are given in Figure 4.14. As segments with increased diameter approach to extension-tool contact, the shift in the dominant mode reaches to almost 500 Hz. However, decrease in the amplitude of the most flexible mode lowers as segments approach to the tool tip.

The maximum amplitude of the tool tip FRF in the range of 400-800 Hz is given in Figure 4.15. This case differs from the previous two cases since regular decline trend is not observed. The maximum amplitude slightly increases by fluctuating between 20 mm and 38 mm. It reaches to minimum value when segments 6 and 7 have 50 mm diameter and it starts to increase up to 60 mm. Almost 45% improvement in tool tip FRF amplitude is achieved by increasing diameters from 20 mm to 50 mm.

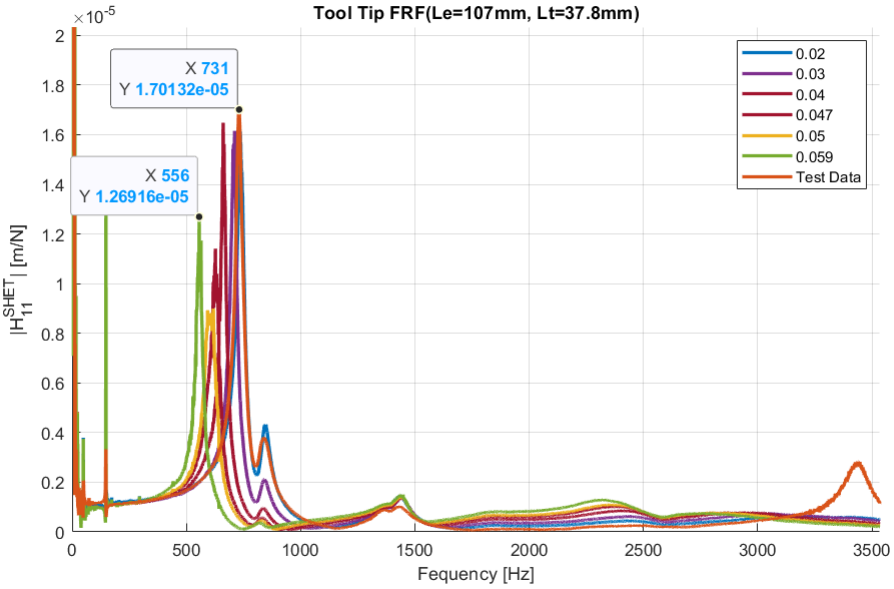


Figure 4.14: Tool Tip FRF with Increased Diameter of Segments 6 and 7

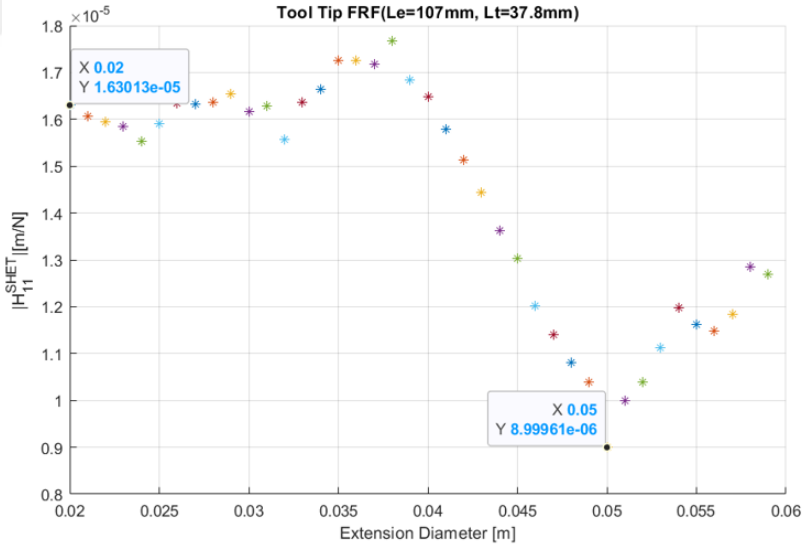


Figure 4.15: Maximum Tool Tip FRF Amplitude with Changing Segment Diameter

Chatter stability calculated for this case is shown in Figure 4.16. SLD is calculated for the case of segments 6 and 7 have 50 mm diameter which provides the minimum amplitude in tool tip FRF.

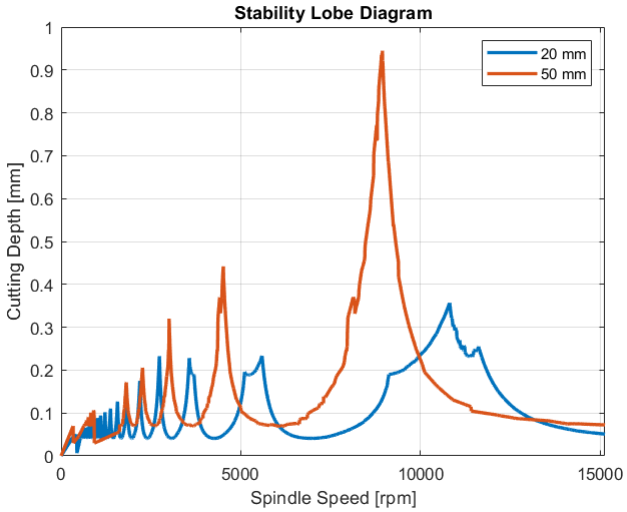


Figure 4.16: Comparison of Stability Lobe Diagrams for Initial Geometry of Extension and Increased Diameter of the Segments 6 and 7 to 50 mm

Similarly, increase in the diameters of the segments leads to improvement in SLD. Even though improvement in the critical depth of cut is not high for the low cutting speeds, significant improvement is obtained between 8000-9000 rpm.

4.2.4 Diameter Increase of Segments 8,9,10 and 11

Effect of the increasing the portion of the extension with larger diameter on the tool tip FRF is investigated in this section. Since the attenuation effect of the segments with larger diameter is more effective at the part of the extension which is closer to the holder contact, segments 8,9,10 and 11 is chosen rather than segments 5,6,7 and 8. Extension model used in this section is shown in Figure 4.17.

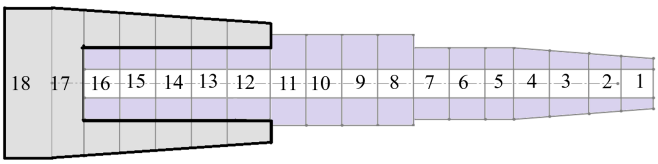


Figure 4.17: Segments of the Extension with Increased Diameter

Change of tool tip FRF with increasing diameter is shown in Figure 4.18.

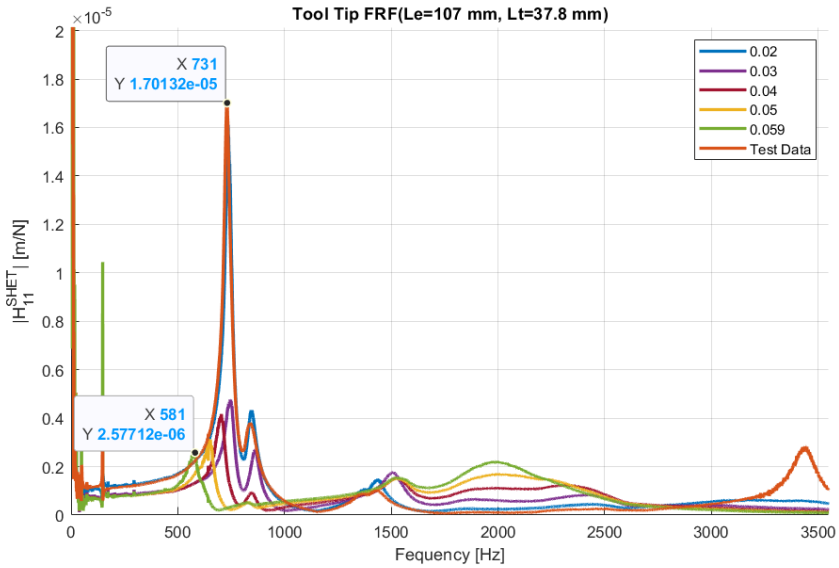


Figure 4.18: Tool Tip FRF with Increased Diameter of Segments 8,9,10 and 11

Similarly, increase in the diameters leads to decrease in the amplitude of the dominant mode and shift to the left of the graph, as expected. The maximum amplitude of the tool tip in the range of 400-800 Hz is obtained while diameters are increased from 20 mm to 60 mm and the results are shown in Figure 4.19.

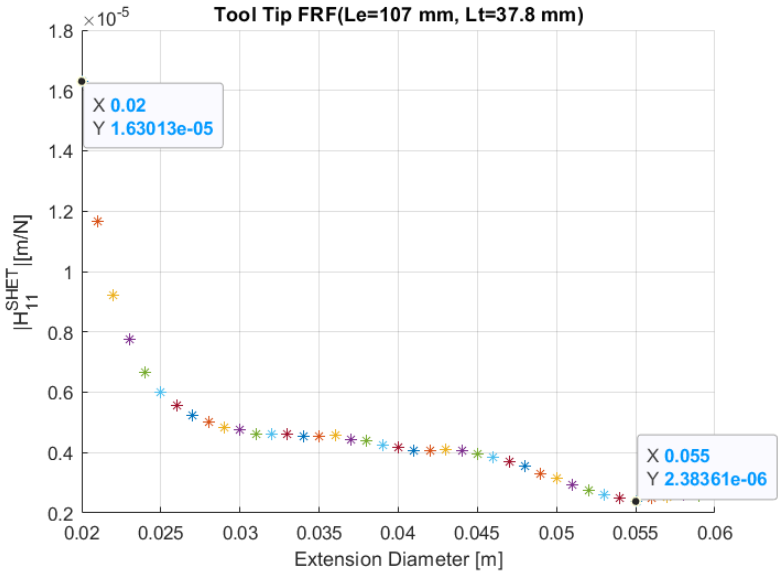


Figure 4.19: Maximum Tool Tip FRF Amplitude with Changing Segment Diameter

Similar trend is observed as in the case of increasing the diameters of segments 10 and 11. However, since diameter of a larger portion of the extension is increased, greater improvement is achieved in terms of the magnitude of the amplitude. 85% drop is obtained when diameters are increased from 20 mm to 55 mm. It can be deduced from Figure 4.19 that changing diameters from 30 mm to 45 mm does not significantly affect the maximum amplitude of the tool tip.

SLD when the diameters of the segments 8, 9, 10 and 11 is increased to 55 mm is given in Figure 4.20. Stable cutting depth is significantly improved when the number of the segments with larger diameter is increased to four. The maximum achievable stable depth of cut is almost doubled between 0-10000 rpm. A dramatic increase is observed in stable cutting region when spindle speed exceeds 10000 rpm.

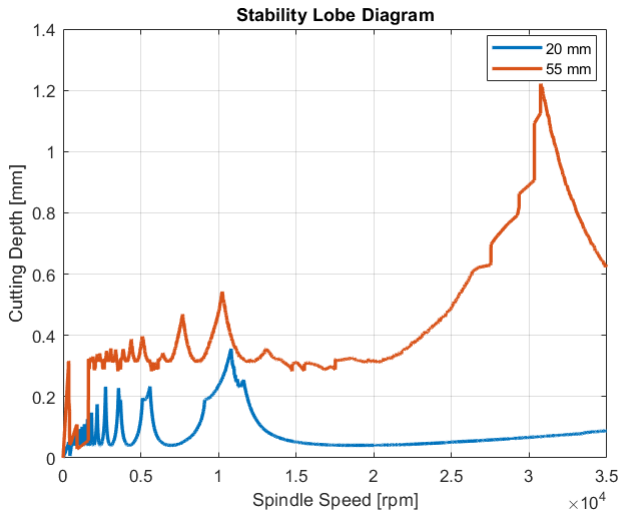


Figure 4.20: Comparison of Stability Lobe Diagrams for Initial Geometry of Extension and Increased Diameter of the Segments 8, 9, 10 and 11 to 55 mm

4.2.5 Diameter Increase of Segments 5 - 11

Increasing the diameter of the all segments which have initially 20 mm is investigated and the segment go under change is shown in Figure 4.21. Change of tool tip FRF with increasing diameter is shown in Figure 4.22.

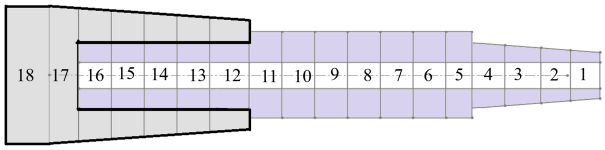


Figure 4.21: Segments of the Extension with Increased Diameter

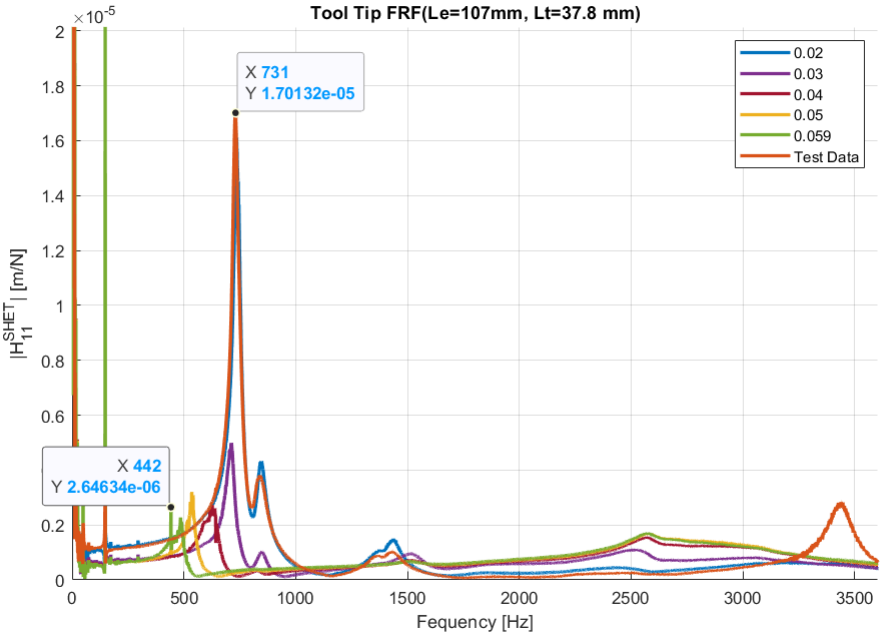


Figure 4.22: Tool Tip FRF with Increased Diameter of Segments 5-11

The dominant mode is reached to almost 400 Hz when diameter of the extension is increased to 60 mm. The change of the maximum amplitude is examined in the range of 400-800 Hz while diameter is increased from 20 mm to 60 mm. The simulations results are shown in Figure 4.23. After 40 mm further increase in diameter is not effective since amplitude change follows a steady trend between 40 mm and 60 mm. Even though the number of segments with larger diameter is increased, only 1% improvement is achieved which leads to 85% drop in amplitude.

Figure 4.24 shows the effect of increasing the diameters of the all segments on chatter stability. It can be deduced that the most improvement on the stable cutting region

is obtained when the all segments which have the same diameter is increase to 60 mm. The maximum achievable critical depth of cut is doubled in between 0-10000 rpm and for the operations in which higher spindle speed is required, results show significant improvement.

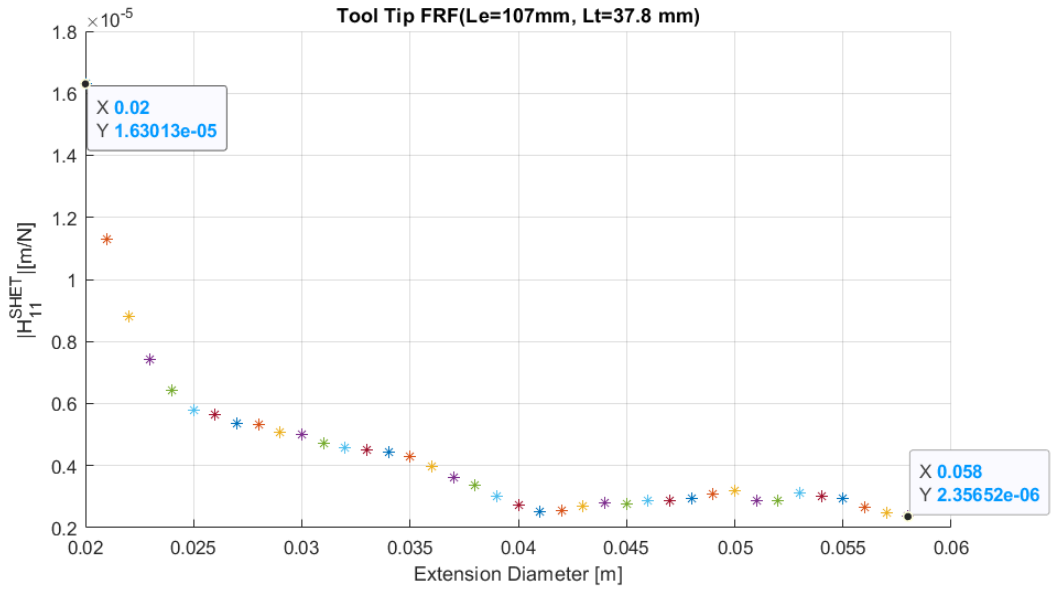


Figure 4.23: Maximum Tool Tip FRF Amplitude with Changing Segment Diameter

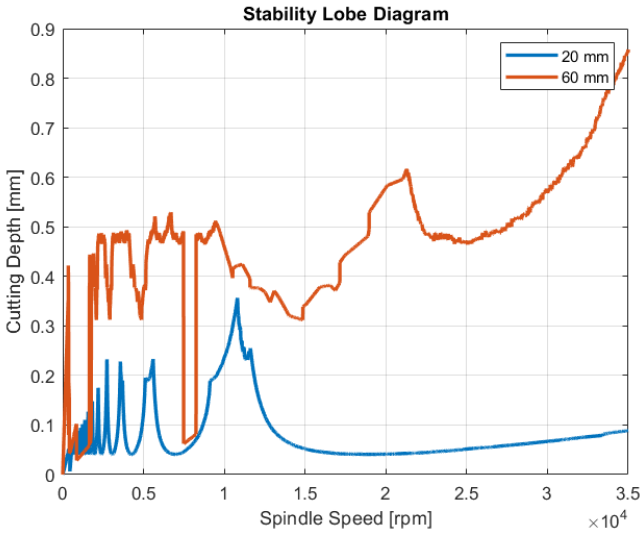


Figure 4.24: Comparison of Stability Lobe Diagrams for Initial Geometry of Extension and Increased Diameter of the All Segments to 60 mm

4.3 Effect of the Tool Overhang Length

In this section, design parameters of the extension is remained unchanged and effects of the tool overhang length is examined. Here, tool overhang length is refer as to non-fluted section of the tool which is added to fluted section measured as 27 mm. Tool tip FRF is calculated for changing tool overhang length between 5-40 mm through simulations. Contacts between holder-extension and extension-tool is modeled as elastic and contact parameters are the same as in Table 4.1 and Table 4.2, respectively. Simulation results are given in Figure 4.25.

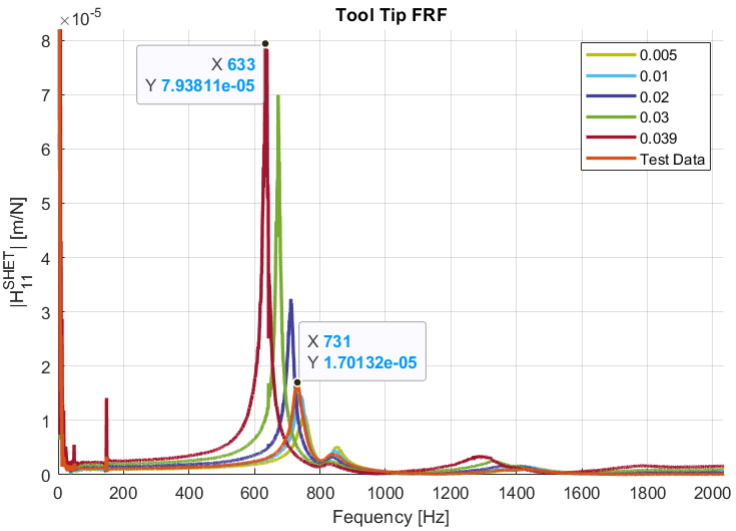


Figure 4.25: Tool Tip FRF Amplitude with Changing Tool Overhang Length

It is seen that as the overhang length is increased, amplitude of the tool tip response increases due to decreasing stiffness of the structure, as expected. For finer examination of the tool overhang length, step size is decreased to 1 mm and the maximum amplitude is searched between the range of 400-800 Hz. Results are given in Figure 4.26. Inclining trend is observed as the overhang length is increased, as expected. Although a slight decline is seen after 36 mm, it is neither significantly drops the amplitude nor it is an continues trend.

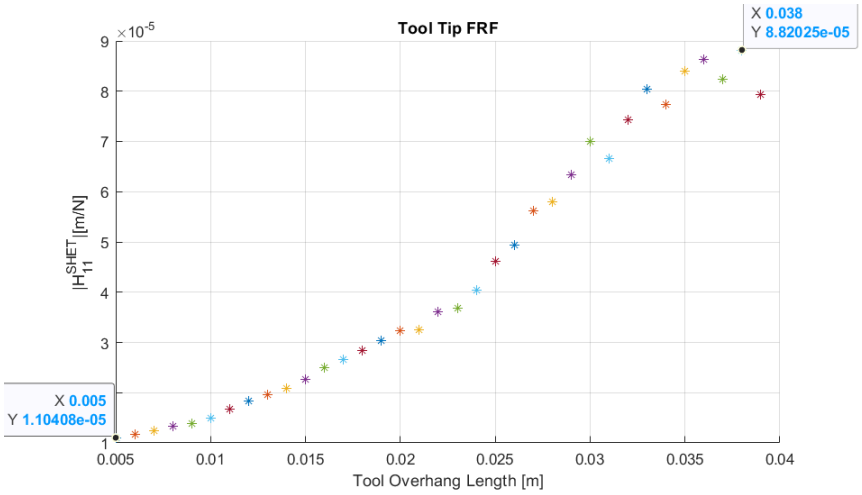


Figure 4.26: Maximum Tool Tip Amplitude with Changing Tool Overhang Length

4.4 Effect of the Simultaneous Change of the Extension and Tool Overhang Length

In this section, decreasing the amplitude of the tool tip FRF is seek by means of simultaneously optimizing the lengths of extension and tool overhang. Figure 4.27 shows maximum amplitude of the tool tip FRF calculated for the each combination of extension and tool overhang length.

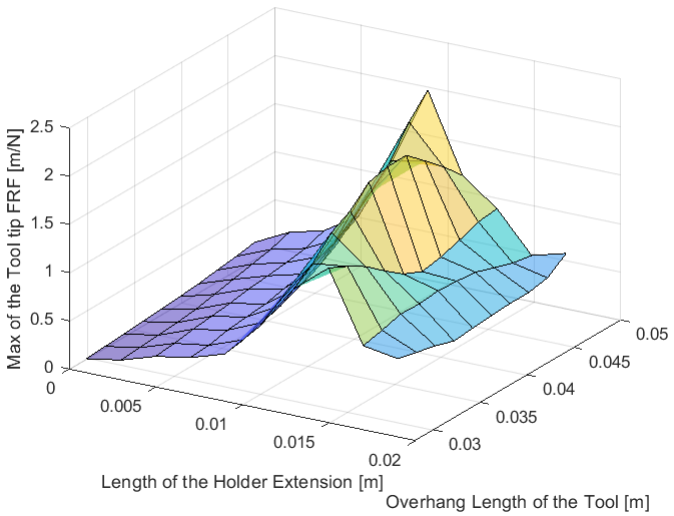


Figure 4.27: Maximum Tool Tip FRF Amplitude obtained for Combinations of Extension Length and Tool Overhang Length

In Figure 4.27, extension length represents the additional length to 97 mm and tool overhang length represents the length of the tool outside the extension. As a result, ranges of the extension and tool overhang length is 97-117 mm and 27-50 mm, respectively. Three cases are encountered that optimally decreases the tool tip amplitude. In the following sub-sections, effects on the tool tip FRFs and SLDs of the cases are explained. SLDs are calculated for slotting operation with 0.2 mm/flute rate, cutting of Al 7050 rigid work-piece with 8 mm tool through CutPro software.

4.4.1 Case 1: Extension Length = 100 mm and Tool Overhang Length = 36 mm

The first case encountered is where the extension length outside the holder is 100 mm and tool length outside the extension is 36 mm when extension diameter is remained unchanged. Figure 4.28 shows comparison of the tool tip FRFs which are calculated for Case 1 and measured experimentally.

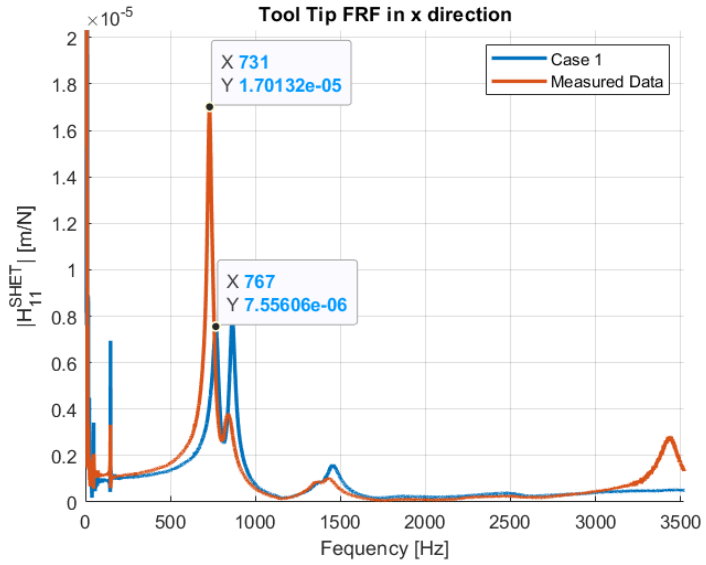


Figure 4.28: Amplitude of Tool Tip FRF for Case 1

As a result of the change in the lengths, the dominant mode is divided into two smaller peaks even though the location of the dominant mode does not significantly change. However, maximum amplitude of the tool tip FRF is decreased about 55.5%.

Increase in the critical depth of cut is not significant until 5000 rpm, however; the

critical depth of cut is increased from 0.05 mm to 0.25 mm and after 11000 rpm it reaches to 0.6 mm as shown in Figure 4.29.

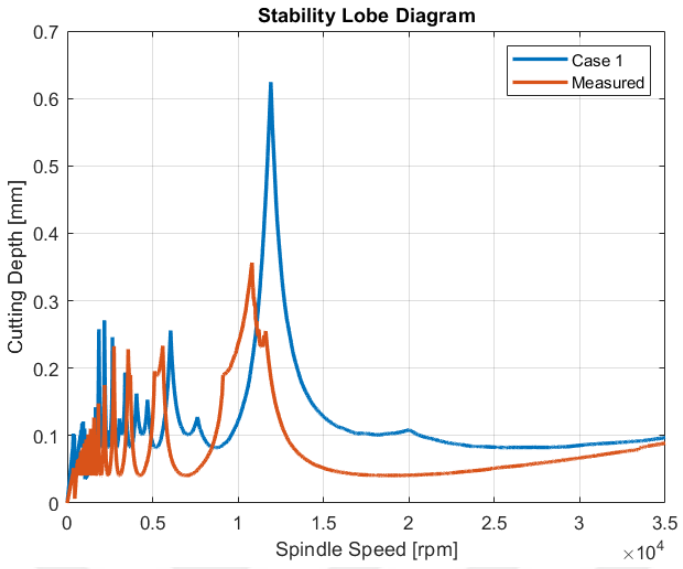


Figure 4.29: Stability Lobe Diagram for Case 1

4.4.2 Case 2: Extension Length = 105 mm and Tool Overhang Length = 28 mm

For the second case, the extension length outside the holder is increased to 105 mm and tool length outside the extension is decreased to 28 mm when extension diameter is remained unchanged. Figure 4.30 shows comparison of the tool tip FRFs of analytically calculated for Case 2 and obtained by initial experimental measurement. Similarly, the dominant mode is divided into to smaller peaks even though the location of the dominant mode only moved from 731 Hz to 766 Hz. However, maximum amplitude of the tool tip FRF is decreased about 57%.

Even though improvement in the chatter-free depth of cut is around 0.05 mm until 6000 rpm, it reaches to 0.25 mm as shown in Figure 4.31. The critical depth of cut reaches to almost 0.7 mm when spindle speed exceeds 12000 rpm.

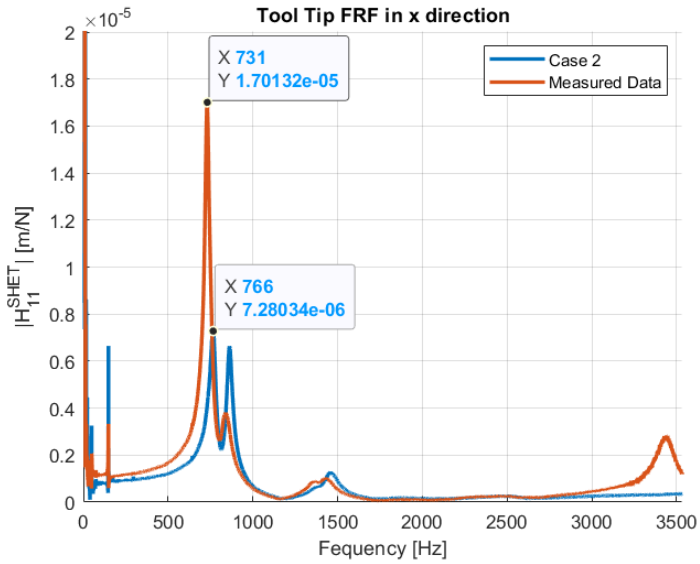


Figure 4.30: Amplitude of Tool Tip FRF for Case 2

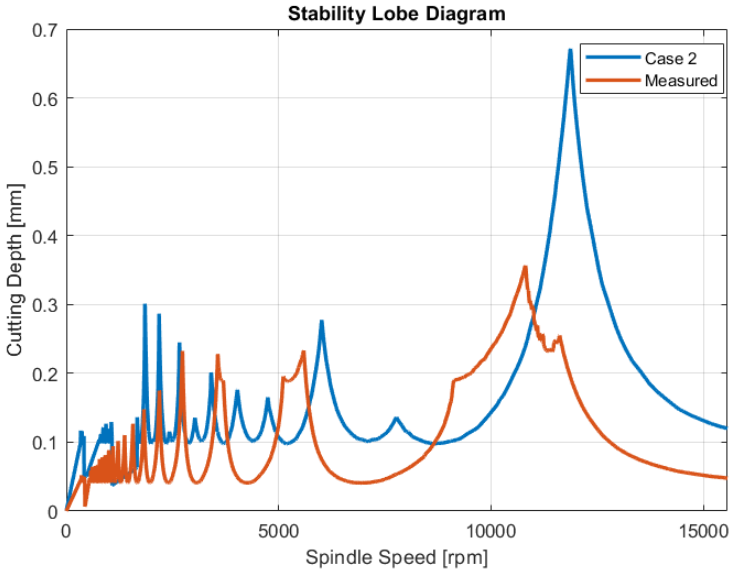


Figure 4.31: Stability Lobe Diagram for Case 2

4.4.3 Case 3: Extension Length = 98 mm and Tool Overhang Length = 40 mm

For the third case, the extension length outside the holder is decreased to 98 mm and tool length outside the extension is increased to 40 mm when extension diameter is remained unchanged. Figure 4.32 shows comparison of the tool tip FRFs which are

calculated for Case 3 and measured experimentally.

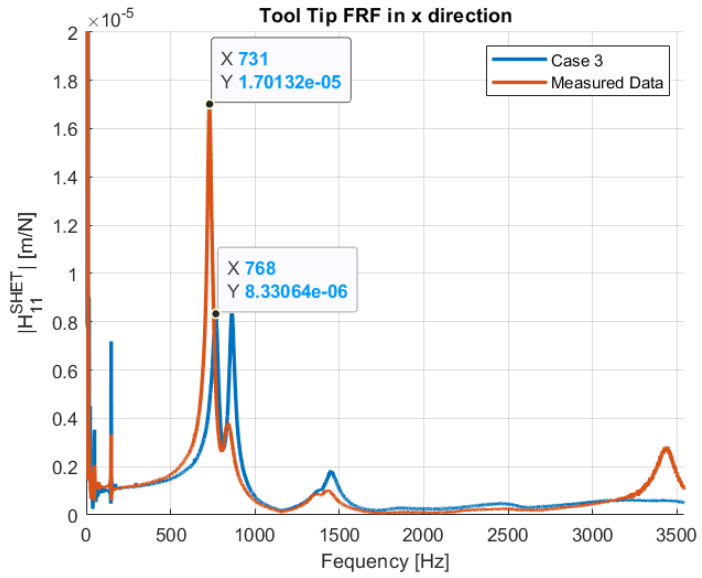


Figure 4.32: Amplitude of Tool Tip FRF for Case 3

Similar to previous cases, the dominant mode is divided into to smaller peaks even though the location of the dominant mode only moved from 731 Hz to 768 Hz. However, maximum amplitude of the tool tip FRF is decreased about 51%.

Figure 4.33 gives the comparison of the SLDs for Case 3 and experimental data.

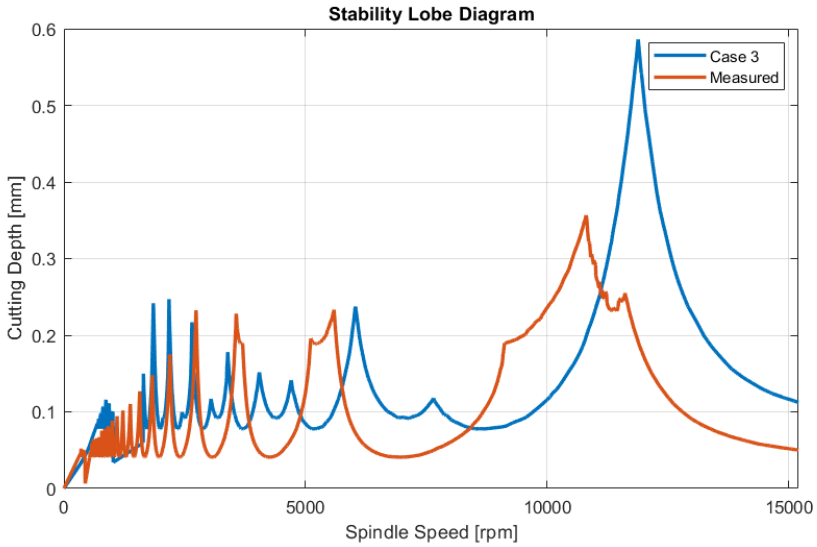


Figure 4.33: Stability Lobe Diagram for Case 3

Increase in the critical depth of cut is about 0.05 mm until 5000 rpm and it reaches to 0.15 mm between 3000-5000 rpm. Significant improvement in the stable cutting region is obtained when the spindle speed exceeds 12000 rpm which enables almost 0.6 mm cutting depth.

As a result, change on the extension diameter dramatically effects the tool tip FRFs therefore stable cutting region and simultaneous modification of the extension length and tool overhang length can improve the dynamics of the machine tool assembly.

CHAPTER 5

SUMMARY AND CONCLUSION

5.1 Summary of the Thesis

In this thesis, analytical optimization procedure of a tool extension component to suppress chatter vibration at the tool tip is studied. This suppression effect is achieved by absorber effect occurring due to overlapping of the modes of the machine tool sub-components. Tuning of the sub-component modes to achieve absorber effect can be obtained by modifying the design parameters of the components. Consequently, amplitude of the tool tip FRF is decreased and stable cutting limit is increased.

Impact testing is applied on the spindle coupled with different holders to obtain holder tip FRFs. The experimentally verified analytical model proposed by Ertürk et al. [9] is utilized for extracting the dynamics of the spindle by decoupling the analytical model of the holders. Identified spindle is re-coupled with analytically modeled holder, extension and tool by using methodology developed by Ertürk et al. [9] to obtain the SHET assembly. Identified dynamics of the spindle is verified through simulations by coupling the spindle with different holders and comparing the experimental results. Shrink fit method is utilized for inserting extension into holder and tool into the extension. Elastic contacts between the holder-extension and extension-tool is also identified. It is found that the dominant mode of the tool tip FRF is controlled by the holder-extension-tool sub-assembly. Therefore; design parameters of the extension and tool is modified in the stage of tuning of tool tip FRF.

First, diameters of the segments in different sections of the extension is increased and effects on the tool tip FRF is observed through simulations. Second, the portion of the extension with larger diameter is increased and finally, effect of the modifying the

diameter of the whole extension is examined. The combination of extension and tool overhang length that minimizes the tool tip FRF is also investigated. As a result, it is found that optimizing design parameters of the components that controls the most flexible mode of the tool tip FRF, leads to attenuation of the dominant mode amplitude and increases the stable cutting limit.

5.2 Conclusions

In this study, dynamics of the spindle is identified based on the spindle-holder impact testing data and the dominant mode of the machine tool assembly is suppress by optimizing the design parameters of the tool extension components. Several cases are studied through simulations and important remarks are summarized below.

- Identifying the spindle dynamics is achieved by subtracting the analytically modeled holder receptance from the spindle-holder FRF data measured by impact testing. Single FRF measurement of a machine tool assembly is adequate for identification of the spindle dynamics and constructing different assemblies by using the analytical models of the sub-components.
- The dominant mode of the SHET assembly is controlled by extension-tool sub-assembly. Therefore, the dominant mode can be suppressed by modifying the design and contact parameters of the extension-tool sub-assembly.
- Although shrink fit method used between the holder-extension and extension-tool which is considered rather stiffer contact, it is found that identifying the elastic contact parameters and including in the SHET assembly provides better agreement with the experiment results.
- Increasing the diameter of the extension attenuates the tool tip FRF as expected. Even though general trend suggests that as the diameter of the extension is increased the amplitude of the dominant mode decreases, it is found that after a certain point increasing diameter does not significantly improves the results.
- It is shown that increasing the diameter of the specific portion of extension also improves the cutting stability and location of that specific portion on the

extension changes the improvement degree which indicates the importance of optimizing the profile of the extension in suppression of tool tip FRF.

- It is shown through simulations that there is not a generalized method to tune chatter frequency of the assembly. Optimal design parameters are searched in a specific range to find the optimal match that minimizes the chatter frequency.

5.3 Future Work

In this thesis, optimization of the design parameters of the extension component and implementing to spindle-holder assembly in order to improve the cutting stability in milling.

This procedure can be investigated further in terms of the extension with different materials and varying the profile of the extension. Furthermore, optimization of the holder geometry can be included in the scope of the study.

In the sensitivity analysis, optimal design parameters are investigated by the modification of two parameters simultaneously. Tuning procedure can be improved by increasing the number of parameters in simultaneous modification.

REFERENCES

[1] J. Munoa, X. Beudaert, Z. Dombovari, Y. Altintas, E. Budak, C. Brecher, and G. Stepan, "Chatter suppression techniques in metal cutting," *CIRP Annals - Manufacturing Technology*, vol. 65, no. 2, pp. 785–808, 2016.

[2] H. E. Merritt, "Theory of Self-Excited Machine-Tool Chatter: Contribution to Machine-Tool Chatter Research—1," *Journal of Engineering for Industry*, vol. 87, pp. 447–454, nov 1965.

[3] S. A. Tobias and W. Fishwick, "A theory of Regenerative chatter," in *The Engineer*, p. 205, 1958.

[4] Y. Altintas and E. Budak, "Analytical Prediction of Stability Lobes in Milling," tech. rep.

[5] T. L. Schmitz, "Predicting high-speed machining dynamics by substructure analysis," *CIRP Annals - Manufacturing Technology*, vol. 49, no. 1, pp. 303–308, 2000.

[6] T. L. Schmitz, M. A. Davies, and M. D. Kennedy, "Tool Point Frequency Response Prediction for High-Speed Machining by RCSA," 2001.

[7] T. L. Schmitz, M. A. Davies, K. Medicus, and J. Snyder, "Improving High-Speed Machining Material Removal Rates by Rapid Dynamic Analysis 1," *CIRP Annals - Manufacturing Technology*, vol. 50, no. 2, pp. 263–268, 2001.

[8] T. L. Schmitz and T. J. Burns, "Receptance Coupling for High-Speed Machining Dynamics Prediction,"

[9] A. E. Ertürk, H. N. Özgüven, and E. Budak, "Analytical modeling of spindle-tool dynamics on machine tools using Timoshenko beam model and receptance coupling for the prediction of tool point FRF," *International Journal of Machine Tools and Manufacture*, vol. 46, pp. 1901–1912, dec 2006.

[10] E. Budak, A. Ertürk, and H. N. Özgüven, "A modeling approach for analysis and improvement of spindle-holder-tool assembly dynamics,"

[11] O. Özşahin, E. Budak, and H. N. Özgüven, "Analytical modeling of the machine tool spindle dynamics under operational conditions," *Proceedings of the 37th International MATADOR 2012 Conference*, pp. 117–120, 2013.

[12] T. L. Schmitz, K. Powell, D. Won, G. Scott Duncan, W. Gregory Sawyer, and J. C. Ziegert, "Shrink fit tool holder connection stiffness/damping modeling for frequency response prediction in milling," *International Journal of Machine Tools and Manufacture*, vol. 47, no. 9, pp. 1368–1380, 2007.

[13] K. Ahmadi and H. Ahmadian, "Modelling machine tool dynamics using a distributed parameter tool-holder joint interface," *International Journal of Machine Tools and Manufacture*, vol. 47, no. 12-13, pp. 1916–1928, 2007.

[14] A. Ertürk, H. N. Özgüven, and E. Budak, "Effect analysis of bearing and interface dynamics on tool point FRF for chatter stability in machine tools by using a new analytical model for spindle-tool assemblies," *International Journal of Machine Tools and Manufacture*, vol. 47, no. 1, pp. 23–32, 2007.

[15] O. Özşahin, A. Ertürk, H. N. Özgüven, and E. Budak, "A closed-form approach for identification of dynamical contact parameters in spindle-holder-tool assemblies," *International Journal of Machine Tools and Manufacture*, vol. 49, no. 1, pp. 25–35, 2009.

[16] O. Özşahin, H.N. Özgüven, and E. Budak, "Estimation of dynamic contact parameters for machine tool spindle-holder-tool assemblies using artificial neural networks," *Proceedings of the 3rd International Conference on Manufacturing Engineering (ICMEN)*, no. October, pp. 131–144, 2008.

[17] R. S. Hahn, "Design of Lanchester Damper for Elimination of Metal-Cutting Chatter," *Journal of Fluids Engineering*, vol. 73, pp. 331–335, apr 1951.

[18] J. Den Hartog, *Mechanical Vibrations*. New York/London: McGraw-Hill Book Company, 1934.

[19] N. D. Sims, “Vibration absorbers for chatter suppression: A new analytical tuning methodology,” *Journal of Sound and Vibration*, vol. 301, pp. 592–607, apr 2007.

[20] Y. Yang, J. Muñoa, and Y. Altintas, “Optimization of multiple tuned mass dampers to suppress machine tool chatter,” *International Journal of Machine Tools and Manufacture*, vol. 50, pp. 834–842, sep 2010.

[21] S. E. Randall, I. B. M. Kingston, and N. Y. D. L. Taylor, “Optimum Vibration Absorbers for Linear Damped Systems,” 1981.

[22] Y. S. Tarng, J. Y. Kao, and E. C. Lee, “Chatter suppression in turning operations with a tuned vibration absorber,” *Journal of Materials Processing Technology*, vol. 105, no. 1, pp. 55–60, 2000.

[23] M. H. Miguélez, L. Rubio, J. A. Loya, and J. Fernández-Sáez, “Improvement of chatter stability in boring operations with passive vibration absorbers,” *International Journal of Mechanical Sciences*, vol. 52, no. 10, pp. 1376–1384, 2010.

[24] J. Tlusty, S. Smith, and W. R. Winfough, “Techniques for the Use of Long Slender End Mills in High-speed Milling,” *CIRP Annals - Manufacturing Technology*, vol. 45, no. 1, pp. 393–396, 1996.

[25] S. Smith, W. R. Winfough, and J. Halley, “The Effect of Tool Length on Stable Metal Removal Rate in High Speed Milling,” vol. 47, pp. 307–310, 1998.

[26] T. L. Schmitz, T. J. Burns, J. C. Ziegert, B. Dutterer, and W. R. Winfough, “Machining Science and Technology An International Journal Tool Length-Dependent Stability Surfaces,” *Tool Length-Dependent Stability Surfaces, Machining Science and Technology*, vol. 8, no. 3, pp. 377–397, 2004.

[27] G. S. Duncan, M. F. Tummond, and T. L. Schmitz, “An investigation of the dynamic absorber effect in high-speed machining,” vol. 45, pp. 497–507, 2005.

[28] A. Ertürk, E. Budak, and H. N. Özgüven, “Selection of design and operational parameters in spindle – holder – tool assemblies for maximum chatter stability by using a new analytical model,” vol. 47, pp. 1401–1409, 2007.

[29] Y. Mohammadi, M. Azvar, and E. Budak, “CIRP Annals - Manufacturing Technology Suppressing vibration modes of spindle-holder-tool assembly through FRF modi fi cation for enhanced chatter stability,” *CIRP Annals - Manufacturing Technology*, vol. 67, no. 1, pp. 397–400, 2018.

[30] T. J. Gibbons, E. Ozturk, L. Xu, and N. D. Sims, “Chatter a voidance via structural modification of tool-holder geometry,” *International Journal of Machine Tools and Manufacture*, vol. 150, mar 2020.

[31] G. Karataş, O. Özşahin, H. N. Özgüven, and E. Budak, “Design optimization of tool holder extension for enhanced chatter stability by using component mode tuning method,” *Procedia CIRP*, vol. 101, pp. 294–297, 2020.

[32] S. Timoshenko, “On the correction for shear of the differential equation for transverse vibrations of prismatic bars,” *The London, Edinburgh, and Dublin Philosophical Magazine and Journal of Science*, vol. 41, pp. 744–746, may 1921.

[33] S. Timoshenko, “On the transverse vibrations of bars of uniform cross-section,” *The London, Edinburgh, and Dublin Philosophical Magazine and Journal of Science*, vol. 43, pp. 125–131, jan 1922.

[34] L. G. Arboleda-Monsalve, D. G. Zapata-Medina, and J. D. Aristizabal-Ochoa, “Timoshenko beam-column with generalized end conditions on elastic foundation : Dynamic-stiffness matrix and load vector,” vol. 310, pp. 1057–1079, 2008.

[35] M. Namazi, Y. Altintas, T. Abe, and N. Rajapakse, “Modeling and identification of tool holder-spindle interface dynamics,” *International Journal of Machine Tools and Manufacture*, vol. 47, no. 9, pp. 1333–1341, 2007.